

## **General Disclaimer**

### **One or more of the Following Statements may affect this Document**

- This document has been reproduced from the best copy furnished by the organizational source. It is being released in the interest of making available as much information as possible.
- This document may contain data, which exceeds the sheet parameters. It was furnished in this condition by the organizational source and is the best copy available.
- This document may contain tone-on-tone or color graphs, charts and/or pictures, which have been reproduced in black and white.
- This document is paginated as submitted by the original source.
- Portions of this document are not fully legible due to the historical nature of some of the material. However, it is the best reproduction available from the original submission.

*TMX-71349*

**ELECTROSTATIC EMISSIONS BETWEEN  
ELECTRON GYROHARMONICS IN THE  
OUTER MAGNETOSPHERE**

**Richard F. Hubbard  
Thomas J. Birmingham**

**May 1977**



**— GODDARD SPACE FLIGHT CENTER —  
GREENBELT, MARYLAND**

(NASA-TM-X-71349) ELECTROSTATIC EMISSIONS  
BETWEEN ELECTRON GYROHARMONICS IN THE OUTER  
MAGNETOSPHERE (NASA) 67 p HC A04/MF A01

N77-27648

CSSL 04A

Unclas  
39019

G3/46

X-602-77-112  
PREPRINT

ELECTROSTATIC EMISSIONS BETWEEN ELECTRON  
GYROHARMONICS IN THE OUTER MAGNETOSPHERE

Richard F. Hubbard\*

Thomas J. Birmingham

May 1977

\*NAS/NRC Resident Research Associate

GODDARD SPACE FLIGHT CENTER  
Greenbelt, Maryland

ELECTROSTATIC EMISSIONS BETWEEN ELECTRON  
GYROHARMONICS IN THE OUTER MAGNETOSPHERE

by

Richard F. Hubbard

Thomas J. Birmingham

ABSTRACT

Electrostatic emissions are often observed by spacecraft in the outer magnetosphere at frequencies between low electron gyroharmonics. The emissions include the well-known odd half-harmonic emissions as well as weaker emissions which occur near the electron plasma frequency. We have constructed a scheme for classifying the emissions and have shown that a theoretical model which has been previously used to explain the "3/2" emissions can be extended to the other classes of emissions. All of the emissions appear therefore to be generated by the same basic mechanism: an unstable electron plasma distribution consisting of cold electrons (<100 eV) and hot loss cone electrons (~1 keV). Each emission class is associated with a particular range of model parameters; the wide band electric field data can thus be used to infer the density and temperature of the cold plasma component. The model predicts that gyroharmonic emissions near the plasma frequency require large cold plasma densities.

## CONTENTS

	Page
ABSTRACT . . . . .	iii
I. INTRODUCTION . . . . .	1
II. TYPICAL ELECTRIC FIELD OBSERVATIONS . . . . .	5
III. THEORY . . . . .	10
IV. SOLUTIONS OF THE PLASMA DISPERSION RELATION . . . . .	18
V. PLASMA MODELS FOR EACH EMISSION CLASS . . . . .	23
VI. THE DIAGNOSTIC USE OF OUR PLASMA MODEL . . . . .	28
VII. CONCLUSIONS . . . . .	33
ACKNOWLEDGMENTS . . . . .	34
REFERENCES . . . . .	35

PRECEDING PAGE BLANK NOT FILMED

## ILLUSTRATIONS

<u>Figure</u>	<u>Page</u>
<p>1 An example of multiple half harmonic emissions observed by Imp 6 at <math>R \approx 9R_E</math> on the day side of the magnetosphere. As many as seven gyroharmonic bands are simultaneously observed. The intense "3/2" emission which occurs between 1 and 2 kHz at 0700 is almost continuously observed from 0500 to 0800. The emissions below 1 kHz are electromagnetic and are not considered in this paper. . . . .</p>	38
<p>2 An example of gyroharmonic emissions occurring near the electron plasma frequency <math>f_p</math>. The shaded region is trapped continuum radiation whose lower cutoff is <math>f_p</math>. Up to three gyroharmonic bands are observed. . . . .</p>	39
<p>3 A comparison between a Maxwellian parallel velocity distribution and the corresponding <math>p^{\text{th}}</math> order Lorentzian distribution. The <math>p = 2</math> Lorentzian has a similar shape for <math>V_{\parallel} \lesssim a_{\parallel}</math> but has more high energy particles than does the Maxwellian. . . . .</p>	40
<p>4 The dependence of the frequency <math>\mu = f/f_g</math> of the fastest growing mode within each gyroharmonic band on the cold plasma density. The parameters <math>\omega_{pH}^2/\Omega^2 = 20</math>, <math>T_c/T_H = 0.04</math>, <math>\theta = 86^\circ</math>, and <math>\Delta = 0</math>. As <math>n_c/n_H</math> increases <math>\mu</math> increases within each band. The highest frequency tracks the cold upper hybrid frequency (dotted line). . . . .</p>	41
<p>5 The dependence of range of the instability within each band on the cold plasma temperature for <math>\beta = 0.5</math>, <math>\Delta = 0</math>, and <math>\mu_{uH}^c = 3.32</math>. The region of unstable frequencies within each band is enclosed by the solid curves, and an asterisk indicates the fastest growing mode within each band as a function of <math>T_c/T_H</math>. The temperature ratio has a considerable effect on the range of the instability. . . . .</p>	42
<p>6 The maximum growth rate <math>\gamma_{\text{max}}</math> within each of the five gyroharmonic bands shown in Fig. 5, plotted against the temperature ratio <math>T_c/T_H</math>. For <math>T_c/T_H \lesssim 0.01</math>, strong growth is seen only in the second and third bands which are closest to <math>\mu_{uH}^c = 3.32</math>. For <math>T_c/T_H \gtrsim 0.04</math>, <math>\gamma_{\text{max}}</math> decreases monotonically with <math>T_c</math> in all bands. . . . .</p>	43

## ILLUSTRATIONS

<u>Figure</u>	<u>Page</u>
<p>7 The effect of the hot plasma density on the range of unstable frequencies. The most unstable frequency is plotted vs. <math>n_c/n_H</math> with <math>T_c/T_H = 0.10</math>, <math>\Delta = 0</math>, and <math>n_c</math> fixed (<math>\mu_{uH}^c = \sqrt{6}</math>). The "error bars" estimate the bandwidth based on the frequency range for which the maximum growth rate <math>\gamma_{max} &lt; 2\gamma(\mu)</math>. The solid, dashed, and dotted curves correspond to <math>\gamma_{max} &gt; 0.01</math>, <math>0.001 &lt; \gamma_{max} &lt; 0.01</math>, and <math>\gamma_{max} &lt; 0.001</math> respectively. Increasing <math>n_H</math> tends to increase <math>\gamma_{max}</math> while leaving frequencies relatively unaffected. . . . .</p>	44
<p>8 A plot of <math>\gamma_{max}</math> vs. fill in factor <math>\Delta</math> in each of the five bands which occur when <math>T_c/T_H = 0.04</math>, <math>\mu_{uH}^c = 3.32</math>, and <math>n_c/n_H = 0.5</math>. Growth rates in all bands decrease monotonically with <math>\Delta</math>, but higher frequency bands are suppressed most severely. . . . .</p>	45
<p>9 Growth rate <math>\gamma</math> vs. frequency <math>\mu</math> for <math>\mu_{uH}^c = 1.34</math>, <math>\beta = 0.1</math> (Curve 1) and <math>\mu_{uH}^c = 1.73</math>, <math>\beta = 0.2</math> (Curve 2) with <math>T_c/T_H = 0.10</math> and <math>\Delta = 0</math>. Unstable waves above <math>\mu = 2</math> can be suppressed by setting loss cone fill in factor <math>\Delta = 0.10</math> (Curves 3 and 4). Hence Curves 3 and 4 reproduce the features of Class 1 (low 3/2) and Class 2 (3/2) emissions. . . . .</p>	46
<p>10 <math>\gamma</math> vs. <math>\mu</math> for <math>\mu_{uH}^c = 3.32</math>, <math>\Delta = 0</math>, <math>\beta = 0.5</math>, and <math>T_c/T_H = 0.10</math>. The frequencies and bandwidths are characteristic of Class 3 (multiple half harmonic) emissions. . . . .</p>	47
<p>11 An example of gyroharmonic emissions near the plasma frequency. Fig. 11a gives <math>\gamma</math> vs. <math>\mu</math> for <math>\beta = 10</math>, <math>\Delta = 0</math>, <math>\mu_{uH}^c = 4.58</math>, <math>f_p/f_g = 4.69</math>, and <math>T_c/T_H = 0.01</math>. The dominant feature is a single strong emission near <math>f_p</math>. In Fig. 11b, <math>T_c/T_H = 0.02</math>, and an emission band above <math>5f_g</math> would be seen. Class 5 emissions include both single band and multiple band emissions near <math>f_p</math>. . . . .</p>	48
<p>12 An estimate, based on solutions to the linear dispersion relation, of the cold upper hybrid frequency <math>\mu_{uH}^c</math> vs. maximum observed frequency <math>\mu_{max}</math>. The "error bars" are uncertainty estimates assuming <math>\Delta &lt; 0.05</math>. This figure can be used to estimate <math>\mu_{uH}^c</math> from electric and magnetic field data whenever emissions of any class are observed. . . . .</p>	49

## ILLUSTRATIONS

<u>Figure</u>		<u>Page</u>
13	The estimates of Fig. 12 converted to $\omega_{pe}^2/\Omega^2$ (or equivalently $n_c$ ) vs. maximum observed frequency $\mu_{max}$ . This figure can be used as a diagnostic tool to estimate the cold plasma density $n_c$ . . . . .	50
14	A plot of 83 individual electric field observations taken at 15 minute intervals from Imp 6 Orbits 178-183 whenever "odd-half-harmonic" emissions are seen. The graph shows the maximum observed frequency $\mu_{max}$ (in units of $f_g$ ) vs. $f_g$ . Higher relative frequencies tend to occur when the magnetic field is weakest, and almost all emissions between $f_g$ and $2f_g$ occur below $1.5f_g$ . The region above the solid curve corresponds to frequencies above 10 kHz and cannot be observed in the data. . . . .	51



# ELECTROSTATIC EMISSIONS BETWEEN ELECTRON GYROHARMONICS IN THE OUTER MAGNETOSPHERE

## I. INTRODUCTION

Banded electrostatic emissions at frequencies above the local electron gyrofrequency  $f_g$  are a prominent and interesting feature of the outer magnetosphere. By far the most common of these emissions are those occurring between  $f_g$  and  $2f_g$ . These were first observed by the plasma wave experiment on Ogo 5 (Kennel, et al., 1970; Fredricks and Scarf, 1973) as narrow band ( $\Delta f/f_g \sim 0.1$ ), large amplitude (1-10 mV/m) waves occurring over the approximate range  $1.25 f_g < f < 1.75 f_g$ . Because this frequency interval is centered at  $1.5 f_g$ , these waves are often loosely termed "3/2" emissions. Similar "3/2" emissions have also been detected by plasma wave experiments on S<sup>3</sup> (Anderson and Maeda, 1977) and Imp 6 (Shaw and Gurnett, 1975). In the Imp 6 experiment "3/2" emissions are sporadically observed on nearly every traversal of the outer magnetosphere: they are indeed also a common magnetospheric feature. It has been suggested that these waves play a dominant role in the precipitation of 1-10 keV electrons (Lyons, 1974; Ashour-Abdalla and Kennel, 1976).

There are several other types of electrostatic turbulence whose characteristics suggest that they are related to "3/2" emissions. There are first of all "n + 1/2" or "odd half harmonic" emissions with n integral and  $> 1$ . Again

the coinage is loose: these are narrow band emissions occurring between  $nf_g$  and  $(n + 1)f_g$  but significantly away from the gyroharmonics themselves. The Ogo 5 experiment occasionally observed "5/2" and "7/2" emissions, and  $(n + 1/2)$  emissions with  $n$  as large as 8 are common in the Imp 6 data, though far less so than the "3/2" emissions.

When " $n + 1/2$ " emissions are seen in the magnetosphere, all half harmonics  $n = 1, 2, \dots, N$  are usually sequentially present. However, Shaw and Gurnett (1975) report narrow band emissions between higher gyroharmonics at times when the "3/2" and other low half harmonics are absent. In such cases, the highest frequency band is often near the local electron plasma frequency  $f_p$ , the latter being determined from the observed lower cutoff of nonthermal continuum radiation (Gurnett and Shaw, 1973).

Somewhat different from the narrow banded emissions discussed so far are "diffuse" band emissions reported by Shaw and Gurnett (1975). These emissions are also confined to bands between the low electron gyroharmonics and tend to occur just outside the plasmopause. They may have substantially wider bandwidths ( $\Delta f \lesssim 0.5 f_g$ ), and much lower intensities than do narrow band emissions. The highest observed frequency of diffuse band emissions is frequently near  $f_p$ .

Banded electromagnetic emissions near  $f_g/2$  have also been reported (Burtis and Helliwell, 1969; Maeda, et al., 1976). These emissions, which are presumably whistler waves, are seldom observed unless "3/2" emissions are

simultaneously present, and a causal link between the two may exist. We shall not be concerned, however, with electromagnetic emissions in this paper.

Part of our task has been to develop a classification scheme for the emissions discussed in the previous paragraphs. Five separate categories of waves have been identified. More importantly, we have developed a parameterized model of a linearly unstable plasma. By suitable choices of the parameters in the model, it is possible to duplicate in a more or less unique fashion the emissions in each category.

The plasma model is essentially the one investigated previously by several other authors (Fredricks, 1971; Young, et al., 1973; Young, 1975; Ashour-Abdalla, et al., 1975; Ashour-Abdalla and Kennel, 1976). Because of the high frequency of the waves involved, we consider only electron dynamics. There are two electron populations: a "hot" ( $\sim 1$  keV) loss cone component, with density  $n_H$  and parallel and perpendicular temperatures  $T_{\parallel H}$  and  $T_{\perp H}$ , is the source of free energy for the instability. In addition, there are "cold" ( $< 100$  eV) electrons of density  $n_c$  and temperature  $T_c$ . The cold electrons, which originate from the ionosphere, facilitate the propagation of the instability. As might be expected for electrostatic emissions whose frequency is related to  $f_g$ , the waves which we consider propagate nearly perpendicular to  $\vec{B}$ , i. e. the perpendicular and parallel wavenumbers  $k_{\perp}$  and  $k_{\parallel}$  satisfy  $k_{\perp} \gg k_{\parallel}$ .

In this paper, we extend the linear analysis to investigate all types of narrow band electrostatic turbulence observed in the outer magnetosphere. We

feel that diffuse band emissions can also be explained by this model, but our work here is as yet tentative and will be reported later. The theoretical analysis of narrow band emissions is coupled to specific Imp 6 electric field observations. The plasma conditions which give rise to emissions in each of the proposed categories are theoretically investigated. We summarize the effects of varying each of the many free parameters in the problem on the morphology of each category of emission. This leads us to a "best estimate" as to local plasma conditions when a given type of emission occurs and hence a predictive or diagnostic capability. In particular, we are able to estimate the local cold plasma density, a parameter which is difficult to measure by direct plasma observations.

## II. TYPICAL ELECTRIC FIELD OBSERVATIONS

The essential features of "half-harmonic" electrostatic emissions are most clearly seen in wide band spectrograms of the type shown in Figure 1. The figure shows time compressed electric field data from the University of Iowa plasma wave experiment on Imp 6 during an outbound orbital pass. Simultaneous magnetic field measurements from the NASA/GSFC magnetometer allow us to calculate  $f_g$ . The most persistent feature is the narrow bandwidth emissions between  $f_g$  and  $2f_g$  which are almost continuously observed from 0500 to 0800. During this time, the relative frequency  $\mu \equiv f/f_g$  of this "3/2" emission varies between 1.2 and 1.45 as the gyrofrequency decreases from 4.6 kHz to 0.92 kHz. Figure 1, however, shows only the last part of this time interval. The "3/2" emissions in Figure 1 are almost constant in frequency and are the dark trace occurring between 1 kHz and 2 kHz.

Higher odd half harmonic emissions occur sporadically after 0655 with as many as seven bands simultaneously present. The precise relative frequencies of the emissions at 0715 --  $f/f_g = \mu = 1.4, 2.3, 3.2, 4.2, 5.2,$  and  $6.1$ -- are indicative of the looseness of the "odd half-harmonic" terminology. The emissions below 1 kHz are the concurrent electromagnetic emissions near  $f_g/2$ .

Figure 2 shows one of the types of emissions reported by Shaw and Gurnett (1975). The sporadic narrow band emissions which first appear about 0525 are the main feature of interest. The shaded region above  $\sim 6$  kHz is the nonthermal

continuum radiation (Gurnett and Shaw, 1973). This radiation is electromagnetic and is density trapped between the plasmopause and the magnetopause. Its lower cutoff is the local electron plasma frequency  $f_p$ . The narrow band emissions here are well above  $f_g$ . The three bands at 0540 are just below  $7f_g$ ,  $8f_g$ , and  $9f_g$ . Although in this case, the frequencies of the narrow band emissions are just below  $f_p$ , similar bands are sometimes observed above the lower continuum cutoff.

Although the continuum radiation is usually observed whenever narrow band emissions of the type shown in Figure 2 are present, the continuum emissions are sometimes missing (e.g., Shaw and Gurnett, 1975, Fig. 4). This may be due to having  $f_p$  exceed the upper frequency limit (10 kHz or 30 kHz) of the wide band spectrometer, but it is more likely that the narrow band emissions are occurring near  $f_p$ , and that the continuum is simply too weak to be observed (R. Shaw, private communication).

The presence of continuum radiation above  $f_p$  is not correlated with the occurrence of electrostatic emissions. Continuum radiation may accompany any type of narrow bandwidth electrostatic emissions, diffuse emissions (e.g., Shaw and Gurnett, 1975, Figs. 6 and 11), or it may even occur in the complete absence of electrostatic turbulence. These properties, plus the fact that the continuum radiation is electromagnetic in nature, suggest that the mechanisms for generating continuum and odd half-harmonic emissions are unrelated.

Based on the work of Shaw and Gurnett (1975) and our own survey of Imp 6 0-10 kHz broadband data, we propose the classification scheme shown in Table 1. With the exception of Classes 1 and 2, the distinction between separate categories is an observationally natural one, and as we shall see, each class corresponds to a different configuration of our plasma model. The original Ogo 5 observations were primarily low latitude measurements and found typical frequencies  $f \sim 1.5 f_g$ , i. e., Class 2 emissions. Our analyses of several orbits of Imp 6 data, however, suggest that  $f_g < f < 2f_g$  waves are concentrated below  $1.2 f_g$ : for example, 60% of the narrow band emissions observed in Orbits 178-183 were Class 1 as opposed to Class 2 emissions. Our theoretical work suggests that this difference in frequency distributions between the Ogo 5 and Imp 6 observations is a latitudinal effect. At the same radial distance from the Earth, the ratio  $f_p/f_g$ , upon which the frequency  $f$  of narrow emissions depends strongly, is smaller at the higher latitudes traversed by Imp 6 (if  $f_p$  is constant or decreases with latitude). Thus, the plasma characteristics of Class 1 and Class 2 events are also different.

Class 3 emissions are multiple " $(n + 1/2)$ " emissions of the type shown in Figure 1. Class 4 emissions are the diffuse electrostatic emissions described by Shaw and Gurnett (1975). Finally, Class 5 emissions are narrow band emissions such as those in Figure 2 between cyclotron harmonics near  $f_p$ .

We have assumed that all Class 5 events have frequencies controlled by cyclotron harmonics even when only a single band near  $f_p$  is observed. It is

possible that some of these emissions are in fact electron plasma oscillations. We shall see that it is theoretically possible to produce gyroharmonic emissions which occur in a narrow band right at  $f_p$ . In principle one should be able to distinguish between electron plasma oscillations and gyroharmonic emissions from the location in time of intensity nulls associated with the spin period of the spacecraft since  $\vec{E}$  is predominantly perpendicular to  $\vec{B}$  for gyroharmonic emissions and parallel to  $\vec{B}$  for electron plasma oscillations. Unfortunately, the Class 5 emissions don't usually show spin modulation (Shaw and Gurnett, 1975). Emissions occurring in two or more bands near  $f_p$ , such as Figure 2, can safely be considered gyroharmonic emissions, while emissions which occur in a single narrow band near the continuum cutoff could be electron plasma oscillations or gyroharmonic emissions. It may be possible to distinguish the two by analyzing electron particle spectra.



TABLE 1

## Classification Scheme for Electrostatic Emissions in the Outer Magnetosphere

Class	Frequency Range	Comments
1. Low "3/2"	$1 < f/f_g \lesssim 1.2, \Delta f/f_g \lesssim 0.1$	Most common emission class for $20^\circ \lesssim  \lambda_m  \lesssim 55^\circ$ .
2. "3/2"	$1.2 \lesssim f/f_g < 2, \Delta f/f_g \lesssim 0.1$	Most widely studied emission class. Probably most common emission class near equator.
3. "n + 1/2" or multiple half harmonic	$f_{\max}/f_g > 2$ $\Delta f/f_g \lesssim 0.1$ in each band	Narrow bandwidth emissions in each gyroharmonic band above $f_g$ up to the $n^{\text{th}}$ band (e.g., Fig. 1).
4. Diffuse band	$f_{\max}/f_g \lesssim 4$ $\Delta f/f_g \sim 0.5$ in lowest band	Less sharply defined emissions in the lowest ( $1 < f/f_g < 2$ ) band. May have emissions in one or two other bands. If continuum observed, $f_{\max} \sim f_p$ .
5. "f ~ f <sub>p</sub> " narrow band	$f_g \ll f_{\max} \sim f_p$ $\Delta f/f_g \lesssim 0.1$	One or more bands near $f_p$ are enhanced. Lower (e.g., "3/2") bands usually missing.

### III. THEORY

The dispersion relation for electrostatic waves in a magnetized electron plasma, where ions form only a fixed neutralizing background, is in cylindrical coordinates, with the z-axis along  $\underline{B}$  (Harris, 1959),

$$0 = 1 - \frac{2\pi}{k^2} \omega_p^2 \int_0^\infty dv_\perp v_\perp \int_{-\infty}^{+\infty} dv_\parallel \sum_{n=-\infty}^{+\infty} \frac{J_n^2(k_\perp v_\perp / \Omega)}{k_\parallel v_\parallel + n\Omega - \omega} \left[ k_\parallel \frac{\partial f}{\partial v_\parallel} + \frac{n\Omega}{v_\perp} \frac{\partial f}{\partial v_\perp} \right] \quad (1)$$

Here  $\omega_p = (4\pi ne^2/m)^{1/2}$  and  $\Omega = |e|B/mc = 2\pi f_g$  are the angular electron plasma and gyrofrequencies respectively and the electron distribution  $f(v_\perp, v_\parallel)$  is normalized to unity

$$2\pi \int_0^\infty dv_\perp v_\perp \int_{-\infty}^{+\infty} dv_\parallel f(v_\perp, v_\parallel) = 1$$

Two different classes of  $f(V_\perp, V_\parallel)$  which lead to unstable solutions ( $\gamma = \text{Im } \omega > 0$ ) to Eq. (1) with  $k_\perp \gg k_\parallel$  have been widely studied. The first type is characterized by an anisotropy in which the temperature  $T_\perp$  associated with the electronic motion perpendicular to  $\underline{B}$  exceeds the equivalent parallel temperature  $T_\parallel$ . While  $T_\perp > 2T_\parallel$  is sufficient for instability in the "3/2" band, the instability is restricted to the region  $3/2 f_g < f < 2f_g$  (Young et al., 1973), and in order to account for observations below  $3/2 f_g$  a complicated non-linear coupling must be invoked (Oya, 1972; 1975).

Instability at higher odd half harmonics requires a still more pronounced temperature anisotropy. It is primarily because such anisotropic distributions

are not observed in the magnetosphere that we analyze this type of distribution function no further.

The second category of distribution functions is one in which  $\partial f/\partial v_{\perp} > 0$  over some region(s) of  $v_{\perp}$ . Only this class of distribution is unstable to strictly flute mode ( $k_{\parallel} \equiv 0$ ) propagation (Baldwin et al., 1969). Pioneering work with this type of distribution was done by Tataronis and Crawford (1970) who investigated the stability of the distribution

$$f = \frac{1}{2\pi v_{\perp}} \delta(v_{\perp} - \alpha_{\perp}) \delta(v_{\parallel}) \quad (2)$$

in an attempt to explain odd half harmonic emissions observed in laboratory devices.

Shortly after the Ogo-5 magnetospheric observations, Fredericks (1971) seized upon the distribution Eq (2) (with a thermal spread in the perpendicular distribution) and was able to show the existence of unstable "3/2" waves propagating within  $10^{\circ}$  of perpendicularity to the field for large but realistic values of  $\omega_p^2/\Omega^2$ . The electrons involved were thought to be "hot" plasma sheet electrons: there was indication that "3/2" emissions are most prevalent during substorm periods when the flux of plasma-sheet-like electrons at Ogo-5 altitudes is enhanced.

Attempts to extend this work to more realistic (loss cone) distribution functions met in failure. Thus loss cone distributions of the Dory-Guest-Harris (DGH) (Dory et al., 1965) type

$$f(v_{\perp}, v_{\parallel}) = \frac{1}{N!(\pi)^{3/2}} \frac{1}{(\alpha_{\perp}^2)^{N+1} \alpha_{\parallel}} v_{\perp}^{2N} \exp - \left( \frac{v_{\perp}^2}{\alpha_{\perp}^2} + \frac{v_{\parallel}^2}{\alpha_{\parallel}^2} \right) \quad (3)$$

were tried and shown to be electrostatically stable unless N became unrealistically large ( $\geq 5$ ) (Dory et al., 1965). It was Young and his coworkers who first recognized the difficulty with small N: in those regions of  $\omega, \underline{k}$  space where the imaginary component of Eq. (1) could be satisfied with  $\gamma = \text{Im}\omega > 0$  (corresponding to instability) the real component of Eq. (1) could not. However, the addition of a small amount of cold plasma to Eq. (3) alleviated the difficulty. The cold component was and is thought to be of ionospheric origin. The admixture which probably exists around  $L \cong 8$  is optimum for instability.

The most recent work in the field, that of Ashour-Abdalla and Kennel (1976, cf. also references therein), also allows partial "fill in" of the loss cone in order to keep growth rates acceptably small. (If growth is too fast, saturation occurs at a low emission amplitude.) Ashour-Abdalla and Kennel thus analyze the stability of the distribution

$$f(v_{\perp}, v_{\parallel}) = \frac{1}{(\pi)^{3/2}} \frac{1}{\alpha_{\perp H}^2 \alpha_{\parallel H}} \left( \Delta + \frac{(1-\Delta)v_{\perp}^2}{\alpha_{\perp H}^2} \right) \exp - \left( \frac{v_{\perp}^2}{\alpha_{\perp H}^2} + \frac{v_{\parallel}^2}{\alpha_{\parallel H}^2} \right) + \frac{\beta}{(\pi)^{3/2} \alpha_{\perp c}^2 \alpha_{\parallel c}} \exp - \left( \frac{v_{\perp}^2}{\alpha_{\perp c}^2} + \frac{v_{\parallel}^2}{\alpha_{\parallel c}^2} \right) \quad (4)$$

This distribution is then the sum of three components: a cold bi-Maxwellian of density  $n_c$ , a hot bi-Maxwellian of density,  $\Delta n_H$ , and a hot  $N = 1$  DGH loss-cone distribution of density  $(1 - \Delta) n_H$ . The ratio  $\Delta/(1 - \Delta)$  between the densities

of hot Maxwellian and loss-cone plasma is referred to as the "fill-in" factor. The ratio  $\beta$  is  $n_c/n_H$  so that in Eq. (1)  $\omega_p^2$  is calculated using the hot plasma density  $n_H$  ( $\omega_p^2$  is then properly  $\omega_{pH}^2$ ). The Ashour-Abdalla and Kennel paper reports on a detailed parameter search for conditions which can produce "3/2" emissions and an analysis of the convective properties of the instabilities. It also contains a somewhat more detailed history of the evolution of theoretical ideas.

Our work extends the plasma parameters search to the frequency regime  $f > 2f_p$ . Since we are concerned with characterizing all categories of odd-half-harmonic emission discussed in Section II, we shall also be considering "3/2" emissions. Our results in this regime generally support the findings of Ashour-Abdalla and Kennel.

We differ from previous work in one major respect: our hot electron distribution parallel to  $\mathbf{B}$  is a Lorentzian of order  $p$ ; thus the distribution function which we analyze is that given by Eq. (4) with the substitution

$$\frac{1}{(\pi)^{1/2} \alpha_{\parallel H}} \exp - (v_{\parallel}^2 / \alpha_{\parallel H}^2) \rightarrow \frac{1 (2p - 2)!! (\alpha_{\parallel H})^{2p-1}}{\pi (2p - 3)!! (v_{\parallel}^2 + \alpha_{\parallel H}^2)^p}$$

(0)!! = (-1)!! = 1

The Lorentzian for several values of  $p$  is plotted in Figure 1 along with the Maxwellian for comparison. Note that as  $p$  becomes very large, the Lorentzian devolves to a  $\delta$ -function at  $v_{\parallel} = 0$ . We have chosen the Lorentzian for two reasons: 1) magnetospheric particle spectra frequently show a "power law" high energy tail (e.g., the spectra shown in Anderson and Maeda, 1977) and

2) the ensuing complexity of the hot contribution to Eq. (1) (of Appendices) is greatly reduced when a Lorentzian is used.

Let us write Eq. (1) symbolically in the form

$$0 = 1 - \frac{\omega_{pH}^2}{\Omega^2} [H_H(\lambda_{\perp}^H, \lambda_{\parallel}^H; \mu) + H_c(\lambda_{\perp}^c, \lambda_{\parallel}^c; \mu)] \quad (5)$$

where

$$\mu = \frac{\omega}{\Omega}, \quad \lambda_{\perp}^{H,c} = \frac{k_{\perp} \alpha_{\perp}^{H,c}}{\Omega}, \quad \text{and} \quad \lambda_{\parallel}^{H,c} = \frac{k_{\parallel} \alpha_{\parallel}^{H,c}}{\Omega}.$$

We adopt the convention that  $k_{\parallel} > 0$ , realizing that symmetric waves having  $k_{\parallel} < 0$  are equally possible. For the instabilities which we investigate in this paper  $\lambda_{\perp H} > 2.5$  and may range as high as 20. In Appendix A we show that for large  $\lambda_{\perp H}$

$$H_H = \frac{1}{\lambda_{\parallel H}^2} \frac{k_{\parallel}^2}{k^2} \frac{2^{p-1} (-1)^{p+1}}{(2p-3)!!} \frac{\partial^{p-1}}{\partial s^{p-1}} \left\langle \frac{1}{\sqrt{s}} \left[ \frac{\sqrt{\pi}}{\lambda_{\perp H}} \exp - \frac{\Gamma^2}{\lambda_{\perp H}^2} \right. \right. \\ \left. \left. \left\langle \lambda_{\parallel H}^2 \left[ \left( 1 - \frac{2\Gamma^2}{\lambda_{\perp H}^2} \right) \left( \frac{1-\Delta}{2} \right) - (1-\Delta) - \Delta \right] \frac{2\pi}{\cos 2\pi\Gamma - 1} + \Gamma \frac{\alpha_{\parallel H}^2}{\alpha_{\perp H}^2} \left[ 2\Delta + (1-\Delta) \left( \frac{2\Gamma^2}{\lambda_{\perp H}^2} - 1 \right) \right] \right. \right. \\ \left. \left. \left[ \frac{\sin 2\pi\Gamma}{1 - \cos 2\pi\Gamma} - \text{ierf} \left( \frac{i\Gamma}{\lambda_{\perp H}} \right) \right] \right\rangle - \frac{2\alpha_{\parallel H}^2}{\alpha_{\perp H}^2} \left[ \Delta + \frac{(1-\Delta)\Gamma^2}{\lambda_{\perp H}^2} \right] \right\rangle \Bigg|_{s=1} \quad (6)$$

Here  $\Gamma(\sqrt{s}) = \mu + i\sqrt{s} \lambda_{\parallel H}$  and  $\text{erf}(z)$  is the (complex) error function

$$\text{erf}(z) = \frac{2}{\sqrt{\pi}} \int_0^z dt \exp - t^2$$

In addition, the validity of our asymptotic procedure in Appendix A requires

$\sigma(\lambda_{\parallel H}) \lesssim \lambda_{\perp H}$  and  $\sigma(\mu) \lesssim \lambda_{\perp H}$ , these conditions being amply satisfied in all our computations. (Note that we can treat  $\mu \sim \lambda_{\parallel H} \sim \lambda_{\perp H}$  provided all are comparably large.)

The computational value of using a Lorentzian parallel distribution should be manifest in Eq. (6): neither sums nor integrations remain; the computationally most difficult component is the error function which is quickly and efficiently evaluated from a series representation; computer complex algebra readily separates  $H_H$  into its real and imaginary parts  $H_{H,real}$  and  $H_{H,imag}$ .

In our investigations we have considered the  $p = 1$  and  $p = 2$  Lorentzians, for which

$$H_H^{p=1} = \frac{1}{\lambda_{\parallel H}^2} \frac{k_{\parallel}^2}{k^2} \tilde{H}_H \quad (7)$$

where  $\tilde{H}_H$  is the quantity in  $\leftarrow \rightarrow$  in Eq. (6) (evaluated at  $s = 1$  so that  $\Gamma = \mu + i\lambda_{\parallel H}$ ) and

$$H_H^{p=2} = \left( 1 - i\lambda_{\parallel H} \frac{\partial}{\partial \mu} \right) H_H^{p=1} \quad (8)$$

Were it necessary or desirable to study situations with yet higher  $p$ , one could continue this procedure and express  $H_H^{p>2}$  completely in terms  $H_H^{p=1}$  and its  $\mu$ -derivatives. These derivatives may in turn be evaluated either numerically or algebraically.

The corresponding cold contribution

$$H_c = -\frac{2\beta k_{\parallel}^2}{\lambda_{\parallel c}^2 k^2} \left\{ 1 + \frac{1}{\lambda_{\parallel c}} \exp - \frac{\lambda_{\perp c}^2}{2} \sum_{n=-\infty}^{+\infty} I_n \left( \frac{\lambda_{\perp c}^2}{2} \right) Z \left( \frac{\mu - n}{\lambda_{\parallel c}} \right) \left[ \mu - n \left( 1 + \frac{\alpha_{\parallel c}^2}{\alpha_{\perp c}^2} \right) \right] \right\} \quad (9)$$

is of a form derived in several places in the literature (e. g. , Ashour-Abdalla et al. , 1975). In Eq. (9)  $I_n$  is a modified Bessel Function of order  $n$  and  $Z$  is the well-known (Fried and Conte, 1961) plasma dispersion function

$$Z(x) = \frac{1}{\sqrt{\pi}} \int_{-\infty}^{+\infty} dt \frac{\exp - t^2}{t - x}$$

While a strictly cold approximation to Eq. (9) is appropriate for some of our computations,  $\lambda_{\parallel c}$  and  $\lambda_{\perp c}$  can in other cases be of  $\mathcal{O}(1)$  so that thermal corrections are important and several terms in the sum need be retained. Even under these conditions, however, the number of computations is fewer than for a "hot" plasma.

In solving Eq. (5) we consider only the situation close to marginal stability so that  $|\mu_i| \ll |\mu_r|$ . Denoting  $H_H + H_c$  by  $H$  we thus solve first the equation

$$1 = \frac{\omega_{pH}^2}{\Omega^2} H_{\text{real}}(\mu_r) \quad (10)$$

in a manner outlined in Appendix B. Here  $H_{\text{real}}$  is, in the usual sense, the real part of  $H$ , given  $\mu$  to be itself real. We then determine a correction  $\Delta\mu$  by solving the quadratic



$$\frac{(\Delta\mu)^2}{2} H''_{\text{real}}(\mu_r) + \Delta\mu H'_{\text{real}}(\mu_r) + i H_{\text{imag}}(\mu_r) = 0 \quad (11)$$

where in Eq. (11) the prime notation is used for differentiation and  $\mu_r$  is that value determined from Eq. (10). Solutions to (11) are complex and thus provide both  $\mu_i$  and a correction to  $\mu_r$ . The quadratic term in Eq. (11) is important only when  $H'_{\text{real}}(\mu_r) \cong 0$ ; when  $H'_{\text{real}}(\mu_r) \cong 1$ , Eq. (11) reduces to the commonly used prescription for calculating weak growth or damping. Having thus solved Eqs. (10) and (11) we check à posteriori that terms in (11) are in fact smaller than those in (10) and that other neglected terms are yet smaller. If this test of smallness fails, the roots are rejected.

#### IV. SOLUTIONS OF THE PLASMA DISPERSION RELATION

Equation (5) is characterized by the following 6 parameters which can be specified independently:  $\frac{\omega_{pH}^2}{\Omega^2}$ ,  $\beta$ ,  $\Delta$ ,  $T_{\parallel H}/T_{\perp H}$ ,  $T_{\parallel c}/T_{\perp c}$ , and  $T_{\parallel c}/T_{\parallel H}$ . It would be an enormous task to examine a significant volume of this 6-dimensional parameter space for instabilities, so we delimit the task somewhat by considering only the "isotropic" case where  $T_{\parallel H} = T_{\perp H} = T_H$  and  $T_{\parallel c} = T_{\perp c} = T_c$ . The gyrofrequency  $\Omega$  scales all frequencies in the problem, and the gyroradius calculated using  $\Omega$  and  $T_H$  is the fundamental unit of length. Our goal in this section is to summarize the gross effects of changing the remaining four parameters on instabilities in the frequency ranges described by our five proposed emission categories. In further discussion we consider the variables in the dispersion equation to be  $\mu$ ,  $\lambda_{\perp H}$  (calling it simply  $\lambda$ ), and  $\theta = \tan^{-1}(k_{\perp}/k_{\parallel})$ .

Fig. 4 displays the frequency  $\mu = \omega/\Omega$  of the fastest growing mode in each gyroharmonic band plotted against  $\beta \equiv n_c/n_H$ . The warm plasma density is constant ( $\omega_{pH}^2/\Omega^2 = 20$ ),  $T_c/T_H = 0.04$ ,  $\Delta = 0$ , and  $\theta = 86^\circ$ . As  $n_c$  increases,  $\mu$  increases within each band, and higher frequency bands may appear. The dotted line indicates the cold upper hybrid frequency defined by

$$\frac{\omega_{uH}^c}{\Omega} \equiv \mu_{uH}^c = \sqrt{1 + \omega_{pc}^2/\Omega^2} = \sqrt{1 + \left(\frac{n_c}{n_H}\right) \left(\frac{\omega_{pH}^2}{\Omega^2}\right)} \quad (12)$$

The fact that instabilities do not occur for  $\mu$ 's much above  $\mu_{uH}^c$  is due to having Re H dominated by the cold electrons for these values of  $\beta$ . Away from exact harmonics of  $\Omega$ , where  $H_{H, \text{imag}}$  is appropriate for instability, propagation in

the limit  $T_c \rightarrow 0$  is possible only at  $\mu_r = \mu_{uH}^c$ . This role of the cold upper hybrid frequency has been investigated by Ashour-Abdalla and Kennel (1976) and Gaffey and LaQuey (1976).

Figure 5 demonstrates the complicated effects of the cold plasma temperature on the range of the instability when  $\mu_{uH}^c > 2$ . Here  $\beta = 0.5$ ,  $\Delta = 0$ , and  $\mu_{uH}^c = 3.32$  (or  $\omega_{pH}^2/\Omega^2 = 20$ ). The range  $2.5 \leq \lambda \leq 12$  and  $82^\circ \leq \theta \leq 89^\circ$  has been sampled, and the region of corresponding unstable  $\mu$ 's is bounded by the solid curves shown. An asterisk indicates the fastest growing mode within each band at the corresponding  $T_c/T_H$  value. For  $T_c/T_H < 0.01$ , note that (a) the lowest band is very narrow and lies close to  $\mu = 2$  and (b)  $\mu_{uH}^c$  is more nearly an absolute upper bound on  $\mu$  than it is at higher  $T_c/T_H$ . For  $T_c/T_H \gtrsim 0.01$ , bands above  $4\Omega$  and  $5\Omega$  become unstable, and the instability width tends to narrow in the second and third bands. The appearance of these higher bands is due to the increase in  $\lambda_c$  with increasing  $T_c$ . As  $\lambda_c$  approaches  $\mathcal{O}(1)$ , thermal effects become important even for the "cold" electrons and several  $I_n(\lambda_c^2/2)$  contribute to the sum in  $H_{c,real}$ . The result is that solutions with  $\mu > \mu_{uH}^c$  are possible.

In addition to shifting the unstable frequency range, the principal effect of increasing  $T_c/T_H$  is to reduce most instability growth rates. Figure 6 plots the maximum growth rate  $\gamma_{max}$  as a function of  $T_c/T_H$  for the parameters of Fig. 5. For  $T_c/T_H \gtrsim 0.04$ , further increases in  $T_c$  tend to stabilize the plasma in all bands. The lack of strong instabilities in the first, fourth, and fifth bands as  $T_c/T_H \rightarrow 0$  occurs because when  $T_c$  is very small, only modes near

$\mu_{uH}^c$  can have large growth rates. The stabilizing effect of the cold plasma temperature arises primarily from the fact that  $H_{c,imag}(\mu) < 0$  always. This gives a Landau damping effect which opposes the  $H_{H,imag}(\mu) > 0$  contribution which drives the instability.

For  $\beta \gtrsim 0.05$ , the real part of the dispersion relation is dominated by the cold plasma component. Increasing  $n_H$  should therefore increase the growth rate  $\gamma$  without changing  $\mu$  by much. This is verified by Fig. 7, which plots the most unstable frequency vs.  $\beta = n_c/n_H$  with  $T_c/T_H = 0.10$ ,  $\Delta = 0$ , and  $\omega_{pc}^2/\Omega^2 = 5$  ( $\mu_{uH}^c = 2.45$ ). The "error bars" delimit the frequency range in which  $\gamma > \gamma_{max}/2$  and hence give an estimate of the bandwidth. The solid, dashed and dotted lines correspond to  $\gamma_{max} > 0.01$ ,  $0.001 \leq \gamma_{max} \leq 0.01$ , and  $\gamma_{max} < 0.001$  respectively. Decreasing  $n_H$  tends to reduce  $\gamma_{max}$  as expected. The small variation in  $\mu$  which does exist is apparently an increase with decreasing  $n_H$ .

We have already discussed the addition of a hot "fill-in" component which reduces the sharpness of the loss cone. Figure 8 shows the maximum growth rate  $\gamma_{max}$  in each band vs.  $\Delta$  for  $\mu_{uH}^c = 3.32$ ,  $n_c/n_H = 0.5$ , and  $T_c/T_H = 0.04$ . Increasing the fill-in factor  $\Delta$  decreases  $\gamma_{max}$  in all bands but tends to affect the higher bands more strongly. In fact, for  $\Delta = 0.05$ , we found no unstable solutions above  $\mu = 5$ . This preferential stabilization of higher frequency bands when the loss cone is filled in is more pronounced for our Lorentzian parallel distribution than it would be for a Maxwellian of comparable temperature. The

fill-in component reduces growth rates because its contribution to  $H_{H,imag}(\mu)$  is always negative.

Figures 4-8 reveal some of the complexities of the dispersion relation. The gross effects of changing each of the major plasma parameters are summarized below based on these Figures and an investigation of a much wider range of parameters.

Cold plasma density. The cold plasma density  $n_c$  primarily determines the cold upper hybrid frequency  $\mu_{uH}^c$  and hence governs the number of unstable frequency bands. The highest unstable frequency  $\mu_{max}$  always lies below  $\mu_{uH}^c$  when  $\mu_{max} < 2$ , but it may be slightly above  $\mu_{uH}^c$  if  $\mu_{max} > 2$ . If a particular band is unstable at some value of  $\mu_{uH}^c$ , the frequencies within that band will increase if  $n_c$  is raised further.

Hot plasma density. The hot plasma provides the free energy to drive the instability. Growth rates tend to increase with  $n_H$ , but the unstable frequency range is largely independent of  $n_H$ .

Cold plasma temperature. The role of  $T_c/T_H$  is a complex one. As  $T_c/T_H \rightarrow 0$ , large growth rates occur in the one or two bands closest to  $\mu_{uH}^c$  while other bands have much smaller growth rates. Low frequency bands (whose frequencies  $\mu$  satisfy  $(\mu_{uH}^c - [\mu]) > 1$ ) occur near the top of the band and have small bandwidths. For  $T_c/T_H \gtrsim 0.01$ , one or two bands above  $\mu_{uH}^c$  may become unstable. At high cold plasma temperatures ( $0.05 \lesssim T_c/T_H \lesssim 0.2$ ), the

unstable frequency range in each band is shifted downward, and all growth rates are reduced. All instabilities disappear for  $T_c/T_H \gtrsim 0.2$ .

Loss cone fill-in. Reducing the slope of  $f_H(v_\perp)$  reduces growth rates in all frequency bands but tends to suppress higher frequency bands much more severely than lower ones.

## V. PLASMA MODELS FOR EACH EMISSION CLASS

In the previous section, we examined the effects of changing various plasma parameters in our model on the solutions to the dispersion relation. We now proceed to use this information to infer plasma conditions which produce instabilities in the appropriate frequency ranges for each category of emission defined in Section II. The fact that we are successful in achieving this goal by variations in a single plasma model strongly supports the validity of the model. This single plasma model hypothesis is also suggested by the fact that there often seems to be a smooth transition in the Imp 6 data from one emission category to another (Shaw and Gurnett, 1975). We feel that the model is sufficiently successful that it can be used in a predictive fashion to infer the unknown cold plasma density and to a lesser extent the cold plasma temperature and loss cone fill-in factor whenever gyroharmonic emissions are observed.

Using Section IV as a guide, we pick for each class of emissions a combination of parameters  $\frac{\omega_{pH}^2}{\Omega^2}$ ,  $n_c/n_H$ ,  $T_c/T_H$ , and  $\Delta$  which produces frequencies and bandwidths characteristic of that category. By varying  $\lambda$  and  $\theta$ , we determine the largest  $\gamma$  corresponding to each unstable  $\mu$  and thus construct curves of maximum growth rate as a function of frequency. These curves should reproduce the features of the emission class while having realistically small growth rates. Using Ashour-Abdalla and Kennel (1976) as a guide, we require temporal growth rates to satisfy  $\gamma \lesssim 0.01$ . Although we have not systematically calculated convective growth rates as was done by Ashour-Abdalla and Kennel, such low

temporal growth rates usually produce realistically small convective growth rates ( $k_i a_1 / \Omega < 1$  where  $k_i$  is the spatial growth rate).

From Figures 4 and 5 and from Ashour-Abdalla and Kennel (1976), the first two classes of emissions ("low 3/2" and "3/2") definitely require

$$\mu_{\max} < \mu_{uH}^c. \quad \text{With somewhat less certainty we also infer that } \mu_{uH}^c \lesssim 2 \text{ and}$$

$$0.05 \lesssim T_c / T_H \lesssim 0.2 \quad \text{when these Class 1 or Class 2 emissions are observed.}$$

Figure 9 represents  $\gamma$  vs.  $\mu$  for  $\mu_{uH}^c = 1.34$  (Curve 1) and  $\mu_{uH}^c = 1.73$  (Curve 2) with  $T_c / T_H = 0.10$  and  $\Delta = 0$ . Both curves show substantial growth rates above  $\mu = 2$  which can be suppressed completely by filling in the loss cone. The small curves (3 and 4) within the growth rate profiles represent the same parameter set with the fill in factor  $\Delta = 0.1$ . Hence, curve 3 represents the growth rate profile for a typical Class 1 ( $\mu_{\max} \leq 1.2$ ) emission while curve 4 represents a Class 2 ( $1.2 \lesssim \mu_{\max} \leq 2$ ) emission. Both curves have small growth rates and narrow bandwidths. The Class 2 or "3/2" emission could be shifted closer to  $\mu = 1.5$  by decreasing  $T_c / T_H$  or increasing  $\mu_{uH}^c$ .

Figure 10 represents an attempt to replicate the features of "multiple half harmonic" or Class 3 emissions. The cold upper hybrid frequency  $\mu_{uH}^c = 3.32$ ,  $\Delta = 0$ ,  $n_c / n_H = 0.50$ , and  $T_c / T_H = 0.10$ . Higher cold plasma densities are required than for "3/2" emissions, and large fill in, which preferentially suppresses the higher frequency modes, cannot be tolerated. The frequencies and bandwidths agree well with those shown in Fig. 1, and the successively smaller



growth rates as one goes to higher bands are in accord with the apparent monotonic decrease in intensity of the bands in Fig. 1. The unstable modes which occur just above  $\mu = 5$  propagate at a more nearly perpendicular angle to  $\vec{B}$  ( $\theta \gtrsim 89^\circ$ ) while lower frequency modes tend to propagate most strongly in the range  $80^\circ \lesssim \theta \lesssim 86^\circ$ . Modes with  $\theta \rightarrow 90^\circ$  have small  $\lambda_{\parallel H}$  and have frequencies very near the gyroharmonics. Instabilities in such modes tend to be stronger with our Lorentzian parallel distribution than with a Maxwellian.

Since Class 4 or diffuse band emissions almost always occur above 10 kHz, and since we have not yet examined any data above 10 kHz, we have not presented a detailed parameterization of such emissions. However, preliminary calculations suggest that diffuse band emissions can also be explained by this same basic electron model, and we are continuing to investigate this possibility.

Class 5 or  $f \sim f_p$  narrow band gyroharmonic emissions can be achieved by this model only if  $n_c \gg n_H$ . This condition arises because the model cannot produce instabilities with frequencies much above  $\mu_{uH}^c$ , and for  $\omega_{pt}^2 = \omega_{pH}^2 + \omega_{pc}^2 \gg \Omega^2$ ,  $\mu_{uH}^c < \sqrt{\omega_{pt}^2/\Omega^2 + 1} \approx \omega_{pt}/\Omega$ . In fact, if the cold upper hybrid frequency is exactly equal to the total plasma frequency ( $\mu_{uH}^c = \omega_{pt}/\Omega$ ), one can easily show that  $\beta = \frac{\omega_{pt}^2}{\Omega^2} - 1$ . It is  $\omega_{pt}$  which is determined from the lower cutoff of the trapped continuum radiation. If  $\mu_{max} = \mu_{uH}^c$  in Fig. 2, then the model requires  $n_c/n_H \approx 80$  since  $f_p \approx 9f_g$ . However, we have seen that if  $T_c > 0$ , frequencies somewhat above the cold upper hybrid can be generated and hence a smaller  $n_c/n_H$  ratio would be permitted. In some cases, gyroharmonic bands similar

to those in Fig. 2 are displaced just above  $f_p$ ; this situation requires a larger  $n_c/n_H$  than the one with gyroharmonic emissions at or just below  $f_p$ .

Figure 11 shows that gyroharmonic emissions at or above  $f_p$  can be produced if  $n_c/n_H$  is sufficiently large. Since there is less free energy available from hot electrons to heat the cold plasma and since large cold plasma densities tend to reduce growth rates, the ratio  $T_c/T_H$  is probably smaller for  $f \sim f_p$  emissions than for "3/2" emissions. In Fig. 11a, in which  $n_c/n_H = 10$ ,  $T_c/T_H = 0.01$ ,  $\Delta = 0$  and  $\mu_{uH}^c = \sqrt{21} = 4.58$ , a single narrow band emission near  $f_p = \sqrt{22} f_g = 4.69 f_g$  is the dominant feature. In Fig. 11b, the cold plasma temperature has been raised to  $T_c/T_H = 0.02$ . An emission band appears above  $\mu = 5$ , the band just below  $\mu = 4$  might also be observable, while the band nearest  $f_p$  has a lower growth rate than in Fig. 11a. This Figure suggests that (a) emissions which are clearly above and separated from  $f_p$ , such as those in Shaw and Gurnett (1975, Fig. 4) are possible with this model and (b) the appearance of two or three bands near  $f_p$  requires a higher  $T_c/T_H$  than a single emission band. Multiple bands just below  $f_p$ , such as those shown in Fig. 2, require a somewhat smaller  $n_c/n_H$  than the value used in Fig. 11 (e.g.,  $n_c/n_H \approx 3$  instead of 10).

The results of this section are summarized in Table 2, which gives a reasonable estimate of the plasma conditions which we believe produce each type of emission. The "3/2" model is in essential agreement with Ashour-Abdalla and Kennel (1976). This Table can be used as a crude diagnostic tool whenever gyroharmonic emissions are observed on a particular spacecraft.

TABLE 2

Proposed Plasma Conditions for Each Class of Electrostatic Emissions

Class	Frequency Range	$\mu_c^{uH} = \sqrt{1 + \omega_{pc}^2 / \Omega^2}$	Comments
1. Low "3/2"	$1 \lesssim f/f_g \lesssim 1.2$	$\frac{f_{\max}}{f_g} < \mu_{uH}^c \lesssim 1.5$	$n_c/n_H \ll 1$ (typically 0.1) $0.05 \lesssim T_c/T_H \lesssim 0.15$ $\Delta \lesssim 0.1$ (some fill in of loss cone distribution)
2. "3/2"	$1.2 \lesssim f/f_g < 2$	$f_{\max}/f_g < \mu_{uH}^c \lesssim 3$	Essentially same as Class 1 but with larger cold plasma density
3. "n + 1/2" multiple half harmonics	$f_{\max}/f_g > 2$	$f_{\max}/f_g \sim \mu_{uH}^c$	$n_c/n_H \lesssim 1$ , $0.05 \lesssim T_c/T_H \lesssim 0.15$ $\Delta \approx 0$
4. "Diffuse band"	$1.5 \lesssim f_{\max}/f_g \lesssim 4$	$f_{\max}/f_g \sim \mu_{uH}^c$ $f_{\max} \sim f_p$ (?)	$n_c/n_H > 1$ (?) $T_c/T_H \sim 0.01$ (?) Requires further study
5. "f ~ f <sub>p</sub> " narrow band	$f_g \ll f_{\max} \sim f_p$	$\mu_c^{uH} \sim f_p$	$n_c/n_H > 1$ ( $\gg 1$ ?) $T_c/T_H \lesssim 0.02$ , $\Delta \approx 0$

## VI. THE DIAGNOSTIC USE OF OUR PLASMA MODEL

We have shown in the last section that each of our 5 categories of odd-half-harmonic waves can be explained by suitable variations of parameters in a single plasma model. Table 2 summarizes the specific values or narrow ranges of  $n_c/n_H$ ,  $T_c/T_H$ , and  $\Delta$  characteristic of each class of emission. We suggest here that gyroharmonic wave observations be used in conjunction with Table 2 and magnetometer measurements of the steady  $B$ -field as a diagnostic tool for determining local plasma parameters. We respond to the potential argument that the observed waves are not generated locally by pointing out that electrostatic oscillations, unlike electromagnetic radiation, are rapidly damped as they propagate into regions which are not at least marginally stable to their growth.

The plasma parameter which is most definitively determined by observing odd-half-harmonic emissions is  $\mu_{UH}^c$ . In this section we shall develop further its relationship to emission frequencies, first by presenting in more detail results of our theory and second by applying these theoretical results to observations, both individual and statistical, made by the Imp-6 experiments. These observations are all consistent with our theory.

While it is sometimes possible to deduce  $n_c$  by measuring  $n_t$  from the continuum cut-off and subtracting the warm plasma density as measured by particle detection experiments (Gurnett and Frank, 1974), this method becomes inaccurate when  $n_c \ll n_H$ . The results of our calculations, previous

theoretical work (Young et al., 1973; Ashour-Abdalla and Kennel, 1976), and the one observation presented by Gurnett and Frank (1974) all suggest that  $n_c/n_H \ll 1$  is a necessary condition for "3/2" emission to occur. Furthermore, the appearance of these "3/2" waves is very common in the outer magnetosphere. We conclude therefore that the use of the subtraction technique to calculate  $n_c$  is frequently a suspect one.

Figure 12 represents our best estimate, based on solutions of the linear dispersion relation, of the cold upper hybrid frequency as a function of the maximum observed frequency of magnetospheric odd-half-harmonic emissions. The "error bars" are uncertainty estimates made under the assumption that the fill in factor  $\Delta$  is  $<.05$  (which in turn assumes that cold plasma heating is the dominant stabilization mechanism (Ashour-Abdalla and Kennel, 1976; Crume, et al., 1972)). For  $\mu_{\max} < 2$ ,  $\mu_{\max} < \mu_{uH}^c$  always so that we can deduce a very accurate lower limit for the cold plasma density. If in fact  $\Delta \gg .05$  then the upper limit is higher, since under such circumstances  $\mu_{uH}^c$  may be large and strong fill in can quench all but the "3/2" emissions. The dip at  $\mu_{\max} \simeq 2$  reflects our computationally observed fact that for Classes 1 and 2,  $\mu_{\max} < \mu_{uH}^c$  (always), while this is not necessarily true if  $\mu_{\max} > 2$  (Classes 3-5). We also observe computationally that  $\Delta$  must be near zero for  $\mu_{\max} \gg 1$  and hence the error estimates in Fig. 12 are quite accurate for large  $\mu_{\max}$ .

The estimates of  $\mu_{uH}^c$  are converted to densities in Fig. 13, using  $\frac{\omega_{pc}^2}{\Omega^2} = (\mu_{uH}^c)^2 - 1$ . Fig. 13 can be used by experimenters to estimate the cold

plasma density whenever gyroharmonic bands are observed. When the continuum cutoff is simultaneously observed, one can estimate  $n_H = n_t - n_c$ . It is usually possible to estimate  $\mu_{\max}$  to within 5% using the electric field data and the measured local magnetic field strength.

We have previously stated that Class 5 ( $f \sim f_p$  gyroharmonic) emissions with  $f_p \gg f_g$  probably require  $n_c \gg n_H$ . Whereas Classes 1-3 emission tend to occur during geomagnetically disturbed times when  $n_c/n_H$  is expected to be small in the outer magnetosphere (cf. Anderson & Maeda, 1977), Classes 4 and 5 are most common during quiet times (Shaw and Gurnett, 1975) when this ratio is more likely to be large, as predicted by our theory. We predict that whenever  $f \sim f_p$  gyroharmonics are observed,  $n_c$  is anomalously high. At such times one would expect that particle detection experiments which measure particles only above some minimum energy threshold can give a significantly lower electron density than the density measured from the trapped continuum lower cut-off. We are currently investigating the data for verification of this hypothesis.

Our discussion of the variation of  $n_c/n_H$  from class to class is pretty much independent of the precise form of the electron distribution function, so long as it has a cold component and is loss cone unstable. Such is not the case with  $T_c/T_H$  and Table 2 should be used with according caution. The hot distribution function, which we have used for our calculations has a loss cone which is unrealistically large for the real outer magnetosphere. A more plausible distribution with a peak in  $f_{LH}$  at a much smaller value of  $v_L$  (relative to  $a_{LH}$ ) can likewise be

unstable (Young et al., 1973). The characteristics of the instability depend strongly on the positive slope ( $\partial f_{\perp} / \partial v_{\perp} > 0$ ) portion of the distribution function and are virtually independent of the tail ( $\partial f_{\perp} / \partial v_{\perp} < 0$ ) so long as it is "gentle." In applying Table 2,  $T_H$  should be interpreted as the effective temperature  $T_{H \text{ eff}} \sim \frac{mv_{\text{max}}^2}{k_B}$  corresponding to the speed at which  $f_{\perp}$  maximizes, since the important low  $v_{\perp}$  region can generally be fit by a DGH distribution of the type we use. An important consequence is that given a hot electron component with a 1 keV thermal spread typical of the plasma sheet,  $T_{H \text{ eff}}$  can be 100 eV or smaller, and hence from Table 2  $T_c \sim 10$  eV, a realistic value for plasma of plasmaspheric or ionospheric origin.

The use of Fig. 13 and Table 2 as a diagnostic tool can be illustrated using Figures 1 and 2. The emissions at 0715 of Fig. 1 are Class 3 (multiple half harmonic emissions) with  $\mu_{\text{max}} = 6.1$  and  $f_g = 1.15$  kHz. (All  $\mu$  values are obtained from the GSFC magnetometer data.) Hence, we estimate  $\omega_{pe}^2 / \Omega^2 \approx 30$  from Fig. 13, and therefore  $n_c \approx 0.5 \text{ cm}^{-3}$ . From Table 2,  $\Delta \approx 0$  and  $0.05 \lesssim T_c / T_H \lesssim 0.2$ . Trapped continuum radiation is not observed, so the total electron density is not available. Figure 2 is a Class 5 emission with  $\mu_{\text{max}} = 8.7$ ,  $f_g = .70$  kHz, and  $f_p = 6.4 \text{ kHz} = 9.1 f_g$  at 0537. Using Fig. 12 as a guide, we estimate  $\mu_{uH}^c \approx 8$ , so  $n_c \approx 0.38 \text{ cm}^{-3}$ . Since the total plasma density (from  $f_p$ ) is  $0.50 \text{ cm}^{-3}$ , the ratio  $n_c / n_H \approx 0.38 / 0.12 \approx 3.2$ . When  $n_c \gg n_H$ , the density ratio predicted by this method is quite sensitive to the estimate of  $\mu_{uH}^c$ . From Table 2, we estimate  $T_c / T_H \sim 0.02$  and  $\Delta \approx 0$ .

Figures 12 and 13 are also supported by a statistical survey of the data taken from a number of orbits. Figure 14 shows as a function of  $f_g$  the highest value of  $f/f_g$  observed during 15 minute intervals from orbits 178 through 183 of Imp-6 whenever odd-half-harmonic waves are present. The data were all taken on the day side of the outer magnetosphere at moderate magnetic latitudes ( $20^\circ \lesssim |\lambda_m| \lesssim 55^\circ$ ). The tendency to see higher relative frequencies when the gyro-frequency is low can be understood if the cold plasma density changes much more slowly than  $f_g$  once the spacecraft is more than  $\sim 1R_E$  beyond the plasmapause. In that case,  $\omega_{pc}^2/\Omega^2$  and hence  $\mu_{uH}^c$  will tend to increase as  $f_g$  decreases, and the theory predicts that higher values of  $\mu$  (and hence more bands) may be observed.

The data used in Fig. 14 also suggests that  $\mu_{max}$  decreases at high magnetic latitudes  $\lambda_m$ . We divided the data into high ( $|\lambda_m| \geq 40^\circ$ ) and low ( $|\lambda_m| < 40^\circ$ ) magnetic latitude cases. 82% (23 of 28) of the high latitude observations were Class 1 ( $\mu_{max} < 1.2$ ) emissions. However, only 53% (29 of 55) of the low latitude observations were Class 1, and all of the Class 3 ( $\mu_{max} > 2$ ) observations were at low latitudes. This effect can be theoretically interpreted using our model. At constant radial distance  $R/R_E$ ,  $f_g$  increases and  $n_c$  is probably constant or decreasing at high latitudes. Hence  $\mu_{uH}^c$  and thus  $\mu_{max}$  would tend to decrease. This probably accounts for the preponderance of Class 1 ( $\mu_{max} \lesssim 1.2$ ) observations in the Imp-6 data. Explorer 45, which always remains at low latitudes, observed more of the traditional  $\mu \approx 3/2$  emissions (R. R. Anderson, private communication).



## VII. CONCLUSIONS

We have conducted a theoretical analysis of the banded electrostatic emissions which occur between consecutive harmonics of  $f_g$  in the outer magnetosphere and have compared our theoretical predictions with Imp 6 electric and magnetic field data. Our results are summarized below.

First, we have constructed a scheme for classifying these emissions (Table 1). Our five categories include the widely studied odd-half-harmonic emissions as well as the waves reported by Shaw and Gurnett (1975). Second, we have extended successfully the linear plasma model of Young, et al. (1973) and Ashour-Abdalla and Kennel (1976), which can explain "3/2" emissions, to the other categories of emissions. Our results indicate that a single plasma model consisting of a hot loss cone electron distribution and a cold electron component can generate instabilities in the frequency ranges appropriate to each category. Hence, all of these emissions appear to arise from the same physical mechanism. Figure 13 and Table 2 can be used as diagnostic guides for estimating the cold plasma density and temperature whenever banded electrostatic emissions are detected. Finally, our results indicate that certain types of emissions require the cold plasma density  $n_c$  to exceed the hot plasma density  $n_H$ . Hence, although the hot loss cone component usually dominates the density in the outer magnetosphere, there are times when  $n_c \gg n_H$ .

## ACKNOWLEDGMENTS

We have made ample use of Imp 6 results from the VLF electric field and magnetometer experiments, and we thank the principal investigators, D. A. Gurnett and N. F. Ness respectively. In addition, we would like to acknowledge useful discussions, advice, and assistance from R. R. Shaw and R. R. Anderson of Iowa, and P. Rodriguez and D. H. Fairfield of GSFC. One of us (R. F. H.) was supported in part by the Atmospheric Research Section, National Science Foundation.

## REFERENCES

- Anderson, R. R., and K. Maeda, VLF emissions associated with enhanced magnetospheric electrons, J. Geophys. Res., 82, 135, 1977.
- Ashour-Abdalla, M., G. Chanteur and R. Pellat, A contribution to the theory of the electrostatic half-harmonic electron gyrofrequency waves in the magnetosphere, J. Geophys. Res., 80, 2775, 1975.
- Ashour-Abdalla, M., and C. F. Kennel, Convective electron loss cone instabilities, U.C.L.A. Report PPG-263, 1976.
- Baldwin, D. E., I. B. Bernstein, and M. P. H. Weenink, Kinetic Theory of Plasma Waves in a Magnetic Field, in Advances in Plasma Physics, Vol. 3 (ed. A. Simon and W. B. Thompson), Interscience, New York, 1969.
- Burtis, W. J., and R. A. Helliwell, Banded chorus: A new type of VLF radiation observed in the magnetosphere by Ogo 1 and Ogo 3, J. Geophys. Res., 74, 3002, 1969.
- Crume, E. C., H. K. Meier, and O. Eldridge, Nonlinear stabilization of single, resonant, loss-cone flute instabilities, Phys. Fluids, 15, 1811, 1972.
- Dory, R. A., G. E. Guest and E. G. Harris, Unstable electrostatic plasma waves propagating perpendicular to a magnetic field, Phys. Rev. Lett., 14, 131, 1965.

- Fried, B. D., and S. D. Conte, The Plasma Dispersion Function, Academic, New York, 1961.
- Fredricks, R. W., Plasma instability at  $(n + 1/2)f_c$  and its relationship to some satellite observations, J. Geophys. Res., 76, 5344, 1971.
- Fredricks, R. W. and F. L. Scarf, Recent studies of magnetospheric electric field emissions about the electron gyrofrequency, J. Geophys. Res., 78, 310, 1973.
- Gaffey, J. D., Jr., and R. La Quey, Upper hybrid resonance in the magnetosphere, J. Geophys. Res., 81, 595, 1976.
- Gurnett, D. A., and L. A. Frank, Thermal and suprathermal plasma densities in the outer magnetosphere, J. Geophys. Res., 79, 2355, 1974.
- Gurnett, D. A. and R. R. Shaw, Electromagnetic radiation trapped in the magnetosphere above the plasma frequency, J. Geophys. Res., 78, 8136, 1973.
- Harris, E. G., Unstable plasma oscillations in a magnetic field, Phys. Rev. Lett., 2, 34, 1959.
- Kennel, C. F., F. L. Scarf, R. W. Fredricks, J. H. McGehee and F. V. Coroniti, 1970, VLF electric field observations in the magnetosphere, J. Geophys. Res., 75, 6136, 1970.
- Lyons, L. R., 1974, Electron diffusion driven by magnetospheric electrostatic waves, J. Geophys. Res., 79, 575, 1974.

- Maeda, K., P. H. Smith, and R. R. Anderson, VLF emissions from ring current electrons, Nature, 263, 37, 1976.
- Oya, H., Turbulence of electrostatic electron cyclotron harmonic waves observed by Ogo 5, J. Geophys. Res., 77, 3483, 1972.
- Oya, H., Plasma flow hypothesis in the magnetosphere relating to frequency shift of electrostatic plasma waves, J. Geophys. Res., 80, 2783, 1975.
- Shaw, R. R., and D. A. Gurnett, Electrostatic noise bands associated with the electron gyrofrequency and plasma frequency in the outer magnetosphere, J. Geophys. Res. 80, 4259, 1975.
- Tataronis, J. A., and F. W. Crawford, Cyclotron harmonic wave propagation and instabilities, J. Plasma Phys., 4, 231, 1970.
- Young, T. S. T., J. D. Callen and J. E. McCune, High-frequency electrostatic waves in the magnetosphere, J. Geophys. Res., 78, 1082, 1973.
- Young, T. S. T., Destabilization and wave-induced evolution of the magnetospheric plasma clouds, J. Geophys. Res., 80, 3995, 1975.

IMP-6  
U OF IOWA PLASMA WAVE EXPERIMENT

ORBIT 178

MARCH 19, 1973

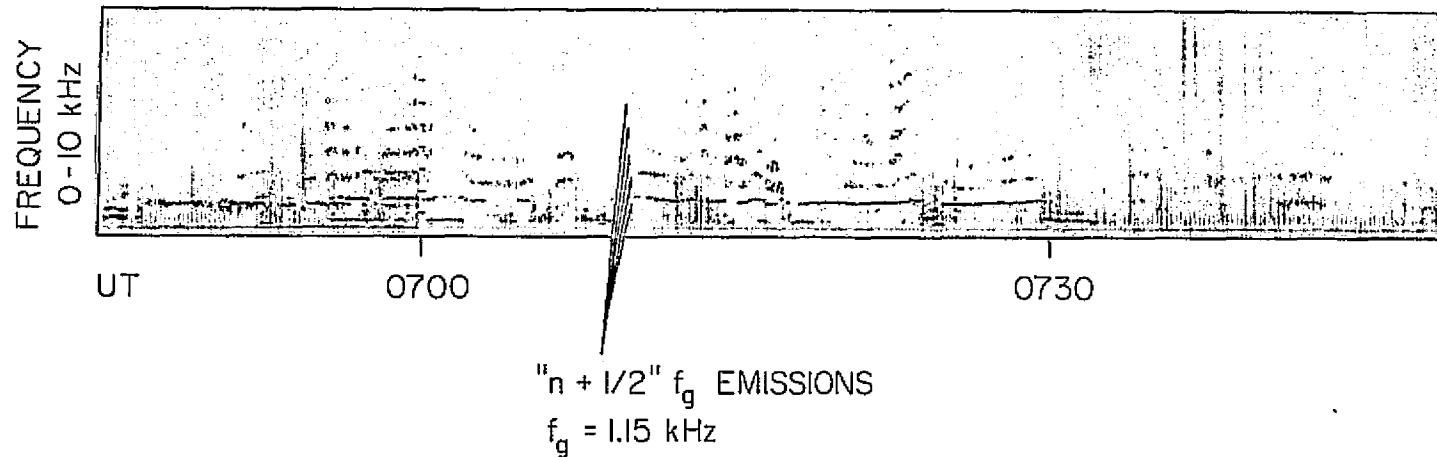


Figure 1. An example of multiple half harmonic emissions observed by IMP 6 at  $R \approx 9R_E$  on the day side of the magnetosphere. As many as seven gyroharmonic bands are simultaneously observed. The intense '3/2' emission which occurs between 1 and 2 kHz at 0700 is almost continuously observed from 0500 to 0800. The emissions below 1 kHz are electromagnetic and are not considered in this paper.

ORIGINAL PAGE IS  
OF POOR QUALITY

IMP-6  
U OF IOWA PLASMA WAVE EXPERIMENT  
ORBIT 84 FEBRUARY 21, 1972

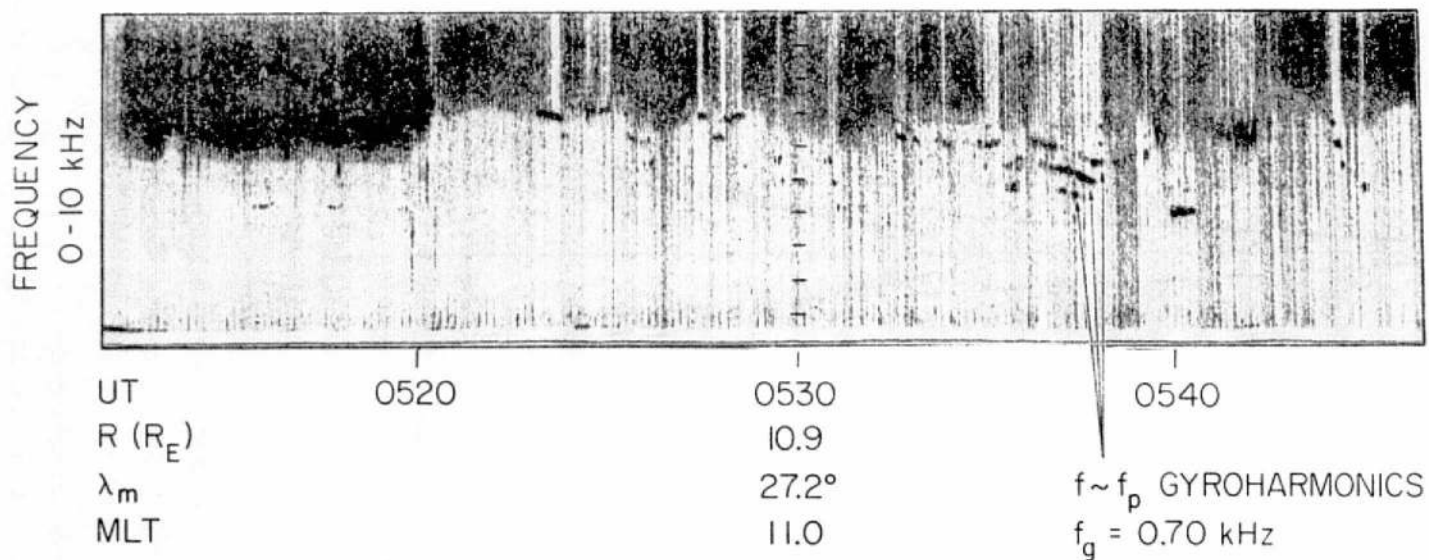


Figure 2. An example of gyroharmonic emissions occurring near the electron plasma frequency  $f_p$ . The shaded region is trapped continuum radiation whose lower cutoff is  $f_p$ . Up to three gyroharmonic bands are observed.

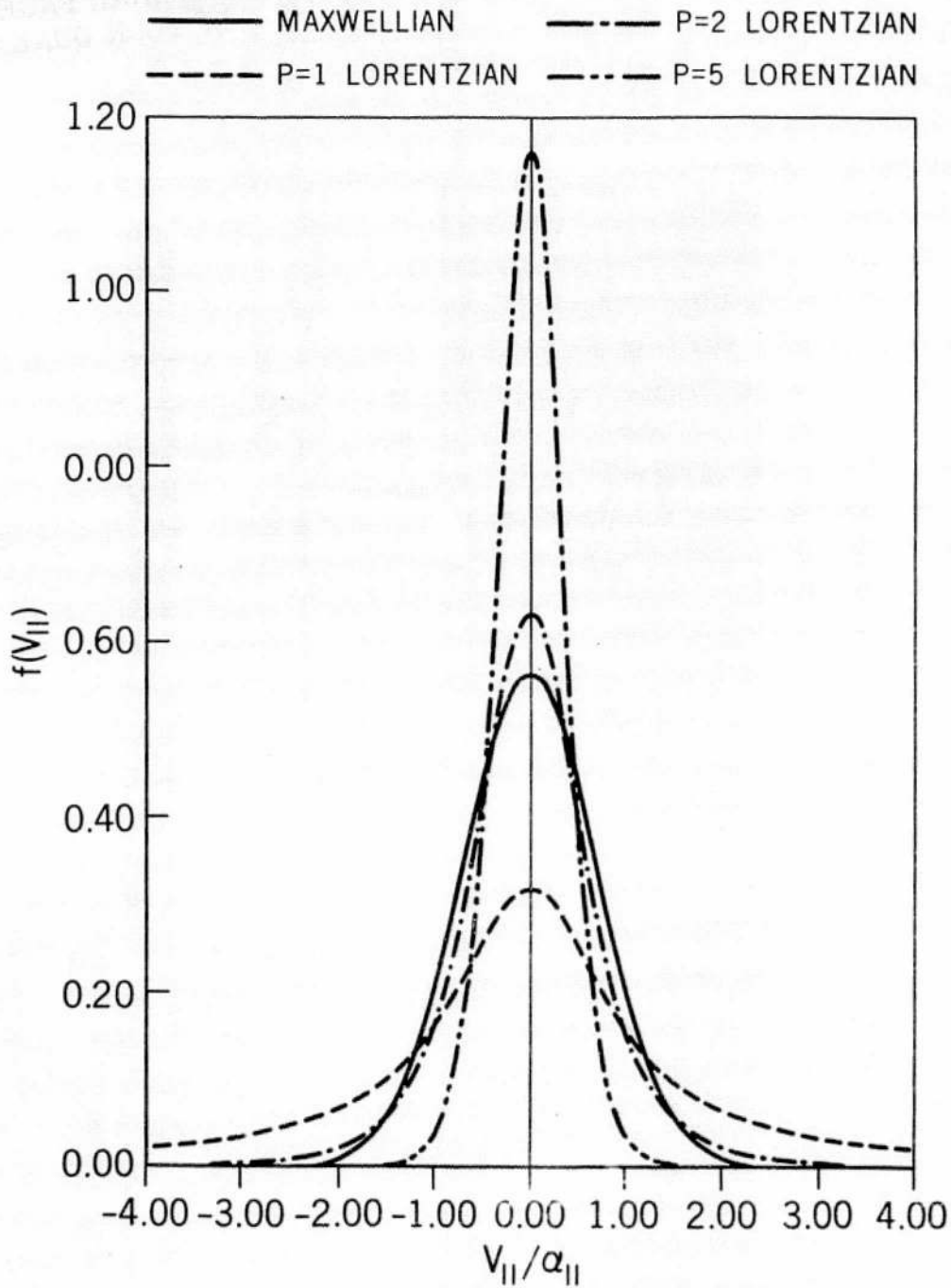


Figure 3. A comparison between a Maxwellian parallel velocity distribution and the corresponding  $p^{\text{th}}$  order Lorentzian distribution. The  $p = 2$  Lorentzian has a similar shape for  $V_{||} \lesssim \alpha_{||}$  but has more high energy particles than does the Maxwellian.



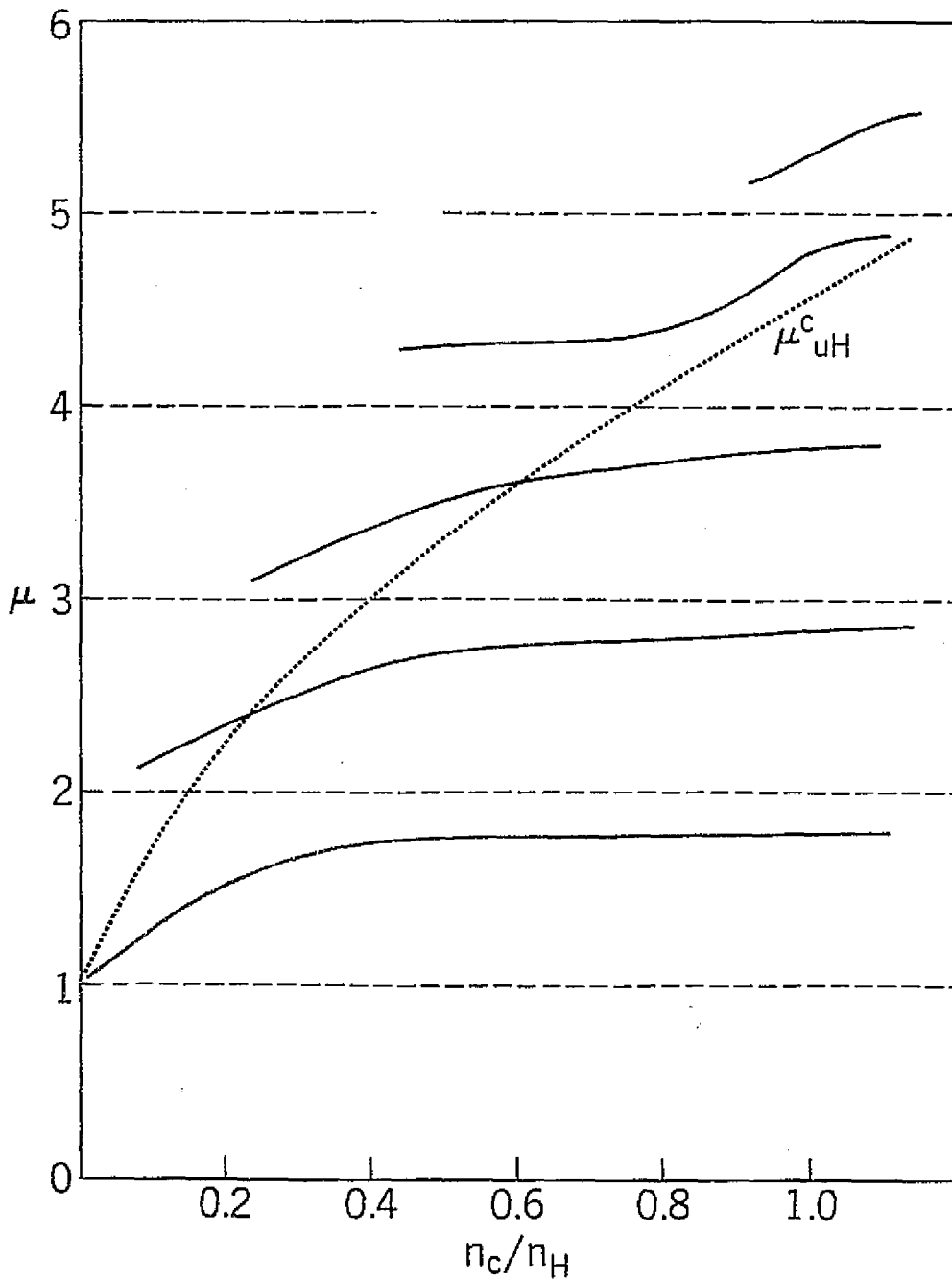


Figure 4. The dependence of the frequency  $\mu = f/f_g$  of the fastest growing mode within each gyroharmonic band on the cold plasma density. The parameters  $\omega_{pH}^2/\Omega^2 = 20$ ,  $T_c/T_H = 0.04$ ,  $\theta = 86^\circ$ , and  $\Delta = 0$ . As  $n_c/n_H$  increases  $\mu$  increases within each band. The highest frequency tracks the cold upper hybrid frequency (dotted line).

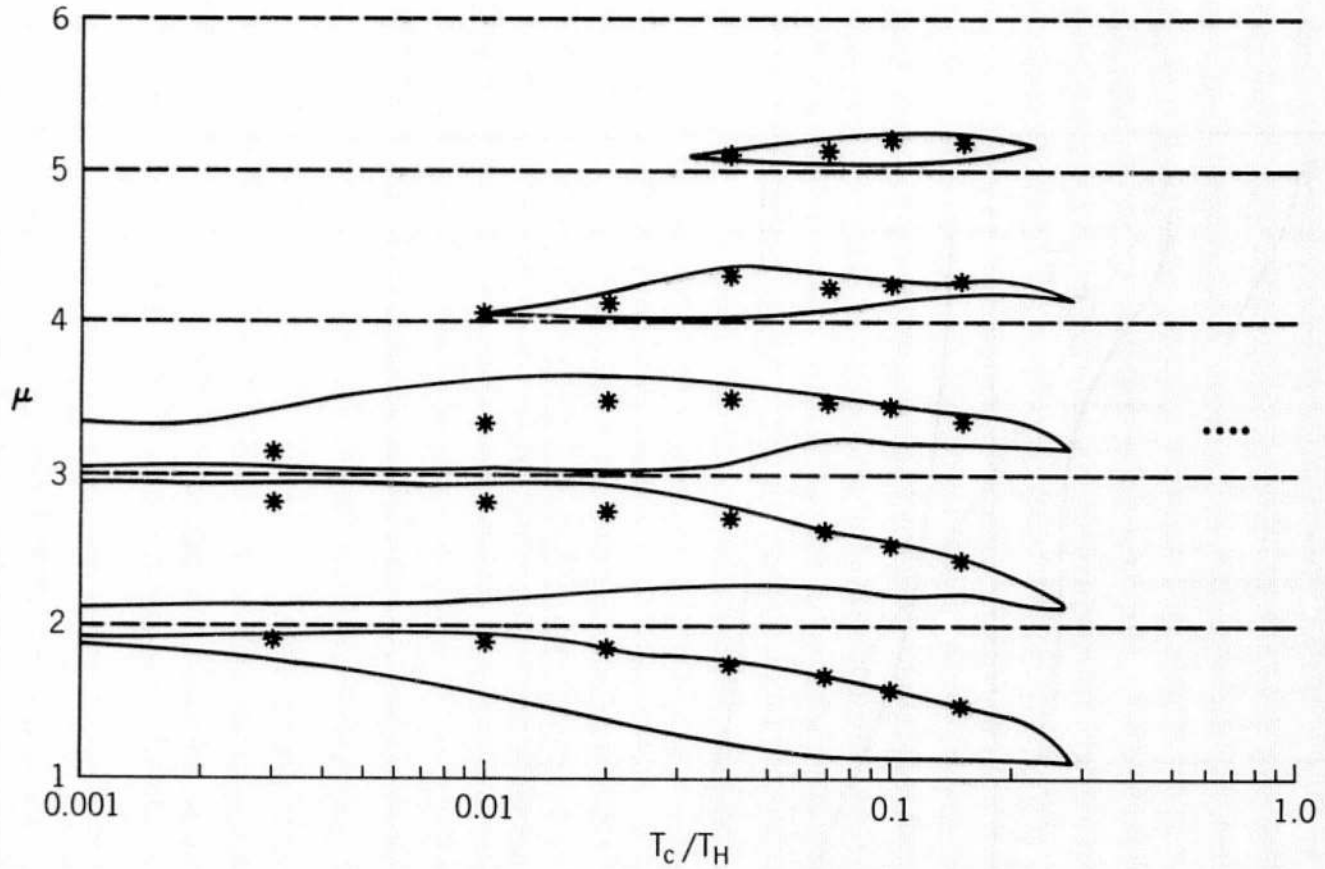


Figure 5. The dependence of range of the instability within each band on the cold plasma temperature for  $\beta = 0.5$ ,  $\Delta = 0$ , and  $\mu_{uH}^c = 3.32$ . The region of unstable frequencies within each band is enclosed by the solid curves, and an asterisk indicates the fastest growing mode within each band as a function of  $T_c/T_H$ . The temperature ratio has a considerable effect on the range of the instability.

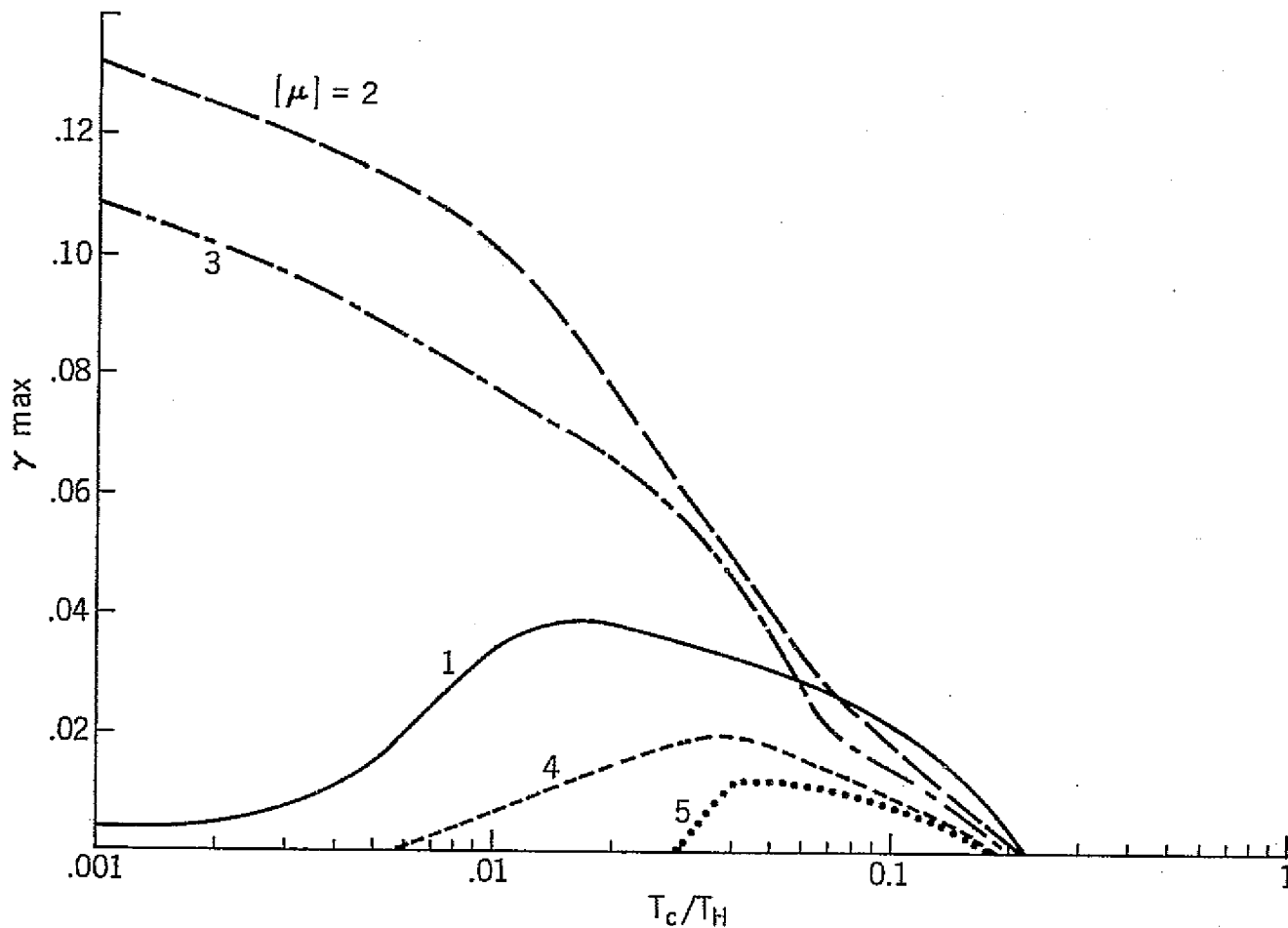


Figure 6. The maximum growth rate  $\gamma_{\max}$  within each of the five gyroharmonic bands shown in Fig. 5, plotted against the temperature ratio  $T_c/T_H$ . For  $T_c/T_H \lesssim 0.01$ , strong growth is seen only in the second and third bands which are closest to  $\mu_{UH}^c = 3.32$ . For  $T_c/T_H \gtrsim 0.04$ ,  $\gamma_{\max}$  decreases monotonically with  $T_c$  in all bands.

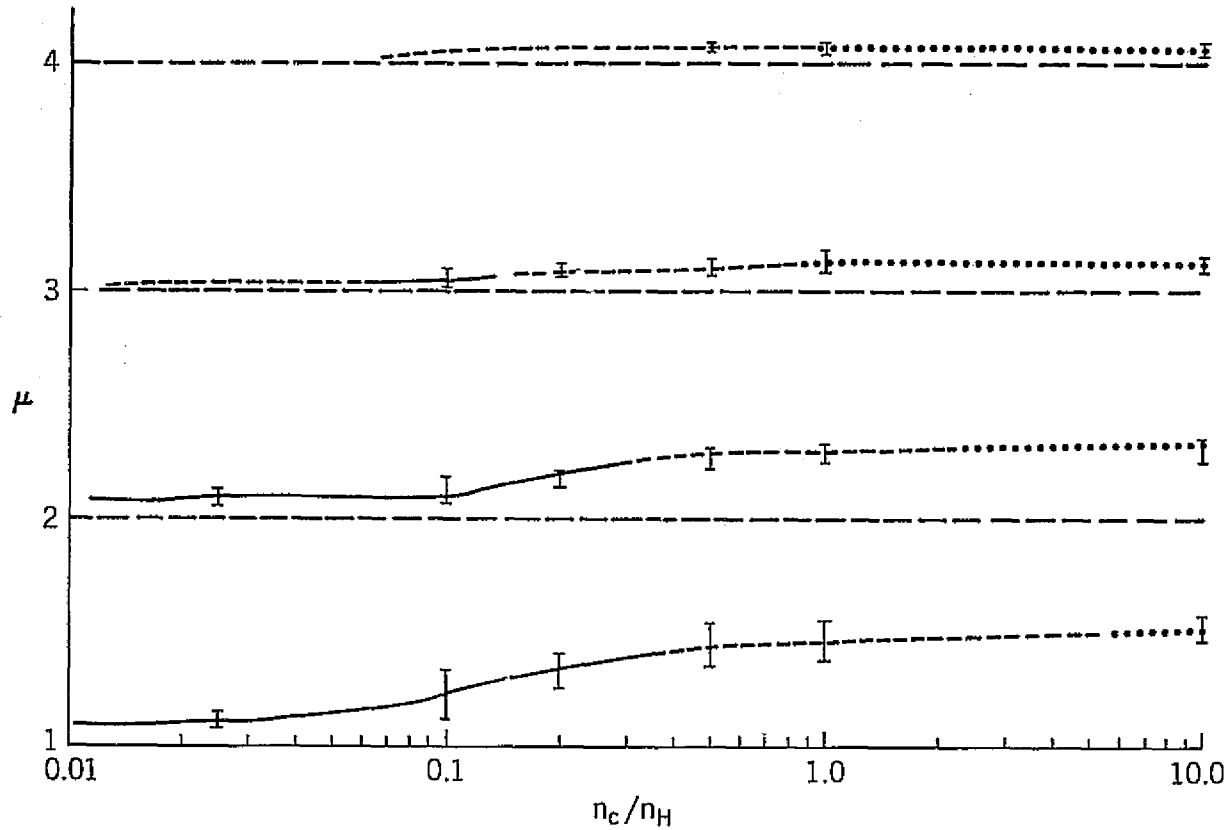


Figure 7. The effect of the hot plasma density on the range of unstable frequencies. The most unstable frequency is plotted vs.  $n_c/n_H$  with  $T_c/T_H = 0.10$ ,  $\Delta = 0$ , and  $n_c$  fixed ( $\mu_{UH}^c = \sqrt{6}$ ). The "error bars" estimate the bandwidth based on the frequency range for which the maximum growth rate  $\gamma_{\max} < 2\gamma(\mu)$ . The solid, dashed, and dotted curves correspond to  $\gamma_{\max} > 0.01$ ,  $0.001 < \gamma_{\max} < 0.01$ , and  $\gamma_{\max} < 0.001$  respectively. Increasing  $n_H$  tends to increase  $\gamma_{\max}$  while leaving frequencies relatively unaffected.

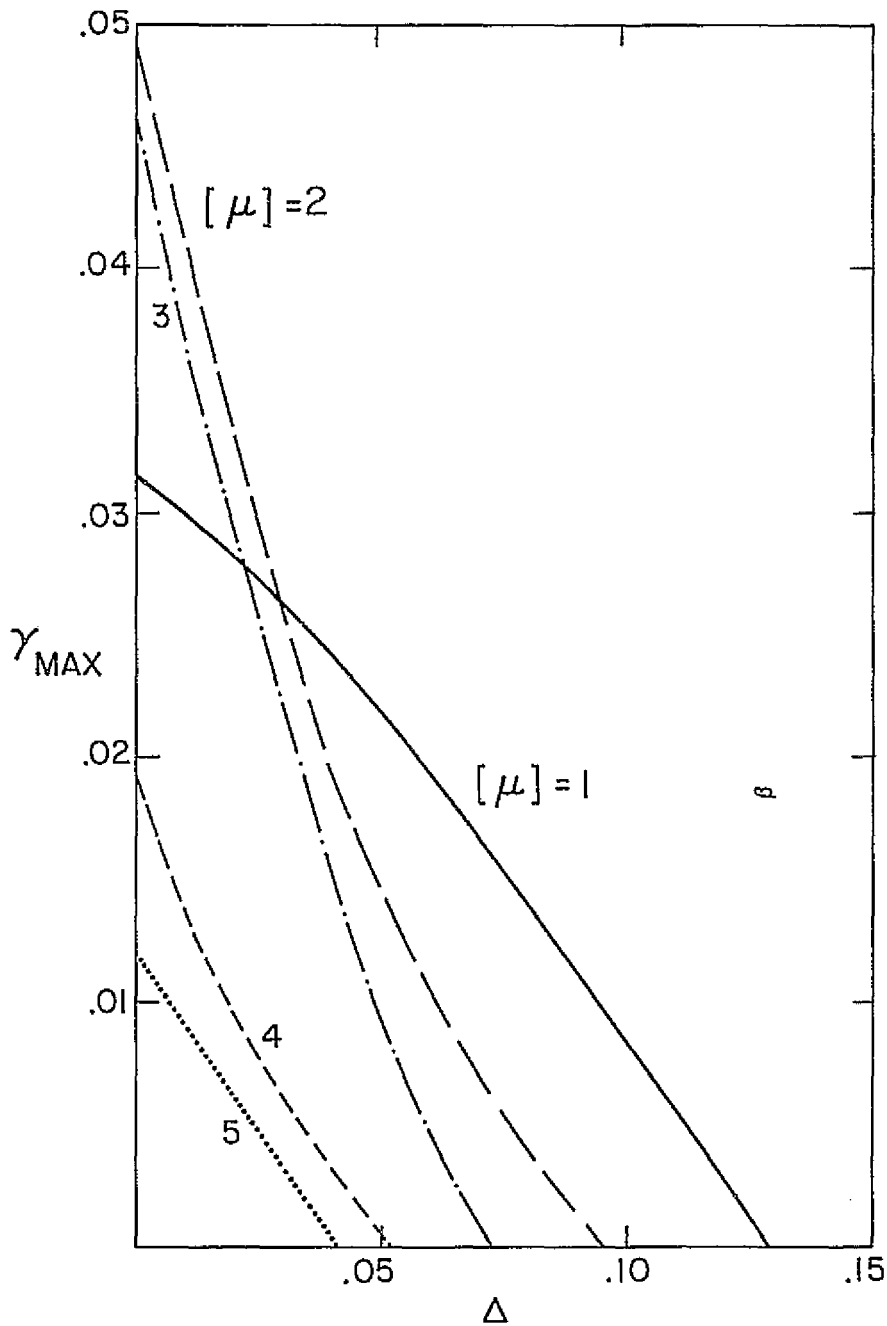


Figure 8. A plot of  $\gamma_{\max}$  vs. fill in factor  $\Delta$  in each of the five bands which occur when  $T_c/T_H = 0.04$ ,  $\mu_{UH}^c = 3.32$ , and  $n_c/n_H = 0.5$ . Growth rates in all bands decrease monotonically with  $\Delta$ , but higher frequency bands are suppressed most severely.

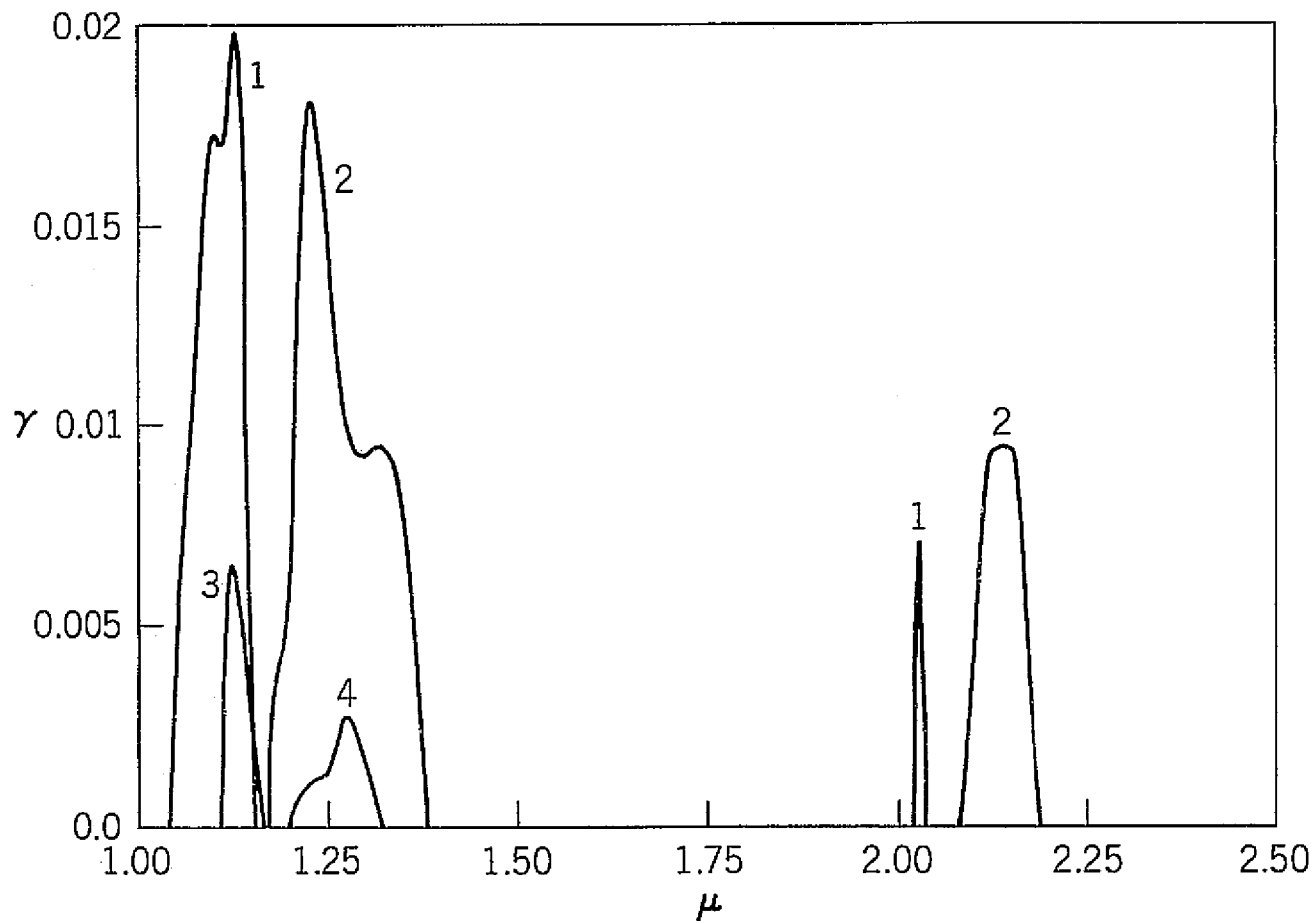


Figure 9. Growth rate  $\gamma$  vs. frequency  $\mu$  for  $\mu_{UH}^c = 1.34$ ,  $\beta = 0.1$  (Curve 1) and  $\mu_{UH}^c = 1.73$ ,  $\beta = 0.2$  (Curve 2) with  $T_c/T_H = 0.10$  and  $\Delta = 0$ . Unstable waves above  $\mu = 2$  can be suppressed by setting loss cone fill in factor  $\Delta = 0.10$  (Curves 3 and 4). Hence Curves 3 and 4 reproduce the features of Class 1 (low 3/2) and Class 2 (3/2) emissions.

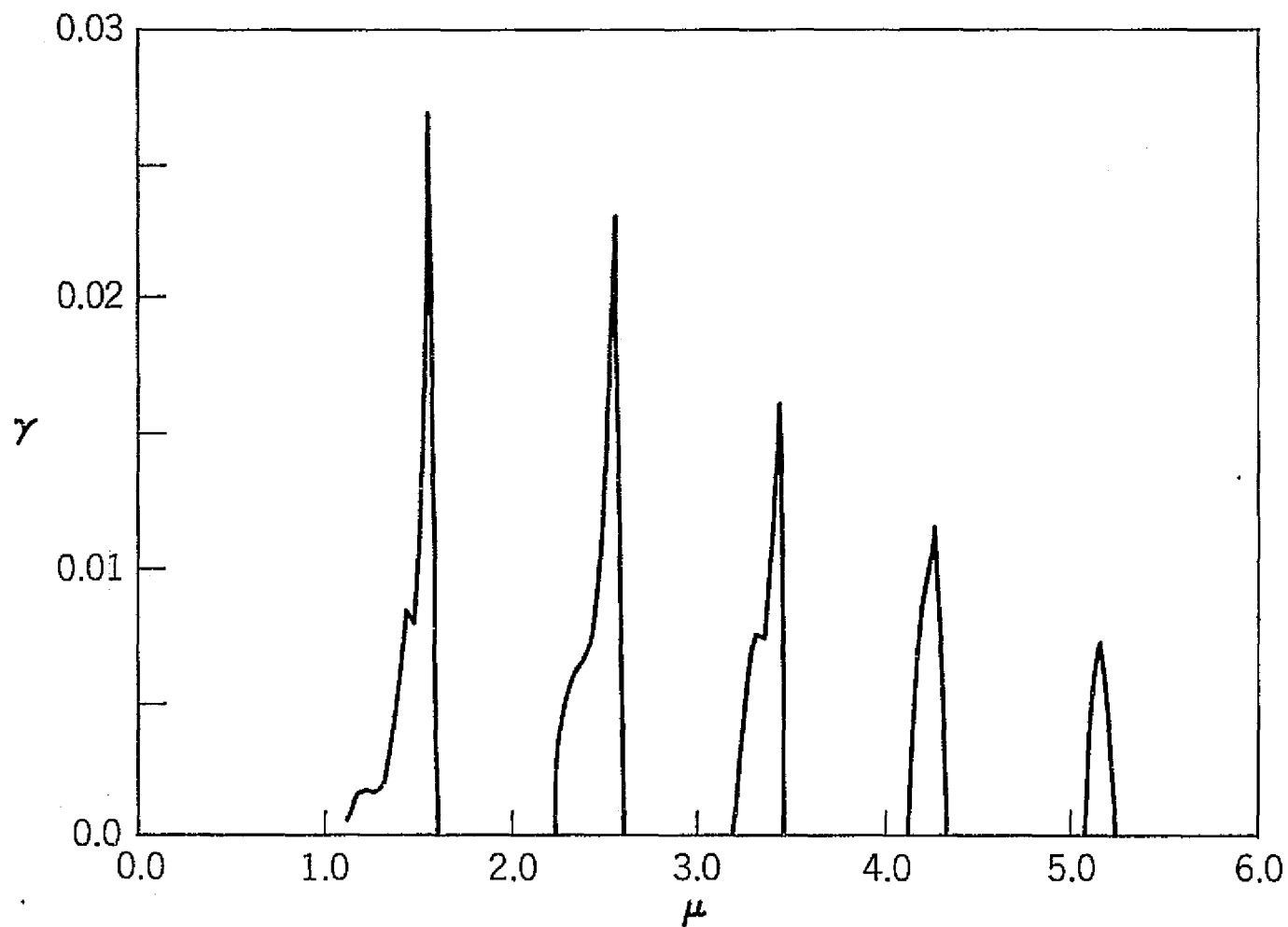


Figure 10.  $\gamma$  vs.  $\mu$  for  $\mu_{UH}^c = 3.32$ ,  $\Delta = 0$ ,  $\beta = 0.5$ , and  $T_c/T_H = 0.10$ . The frequencies and bandwidths are characteristic of Class 3 (multiple half harmonic) emissions.

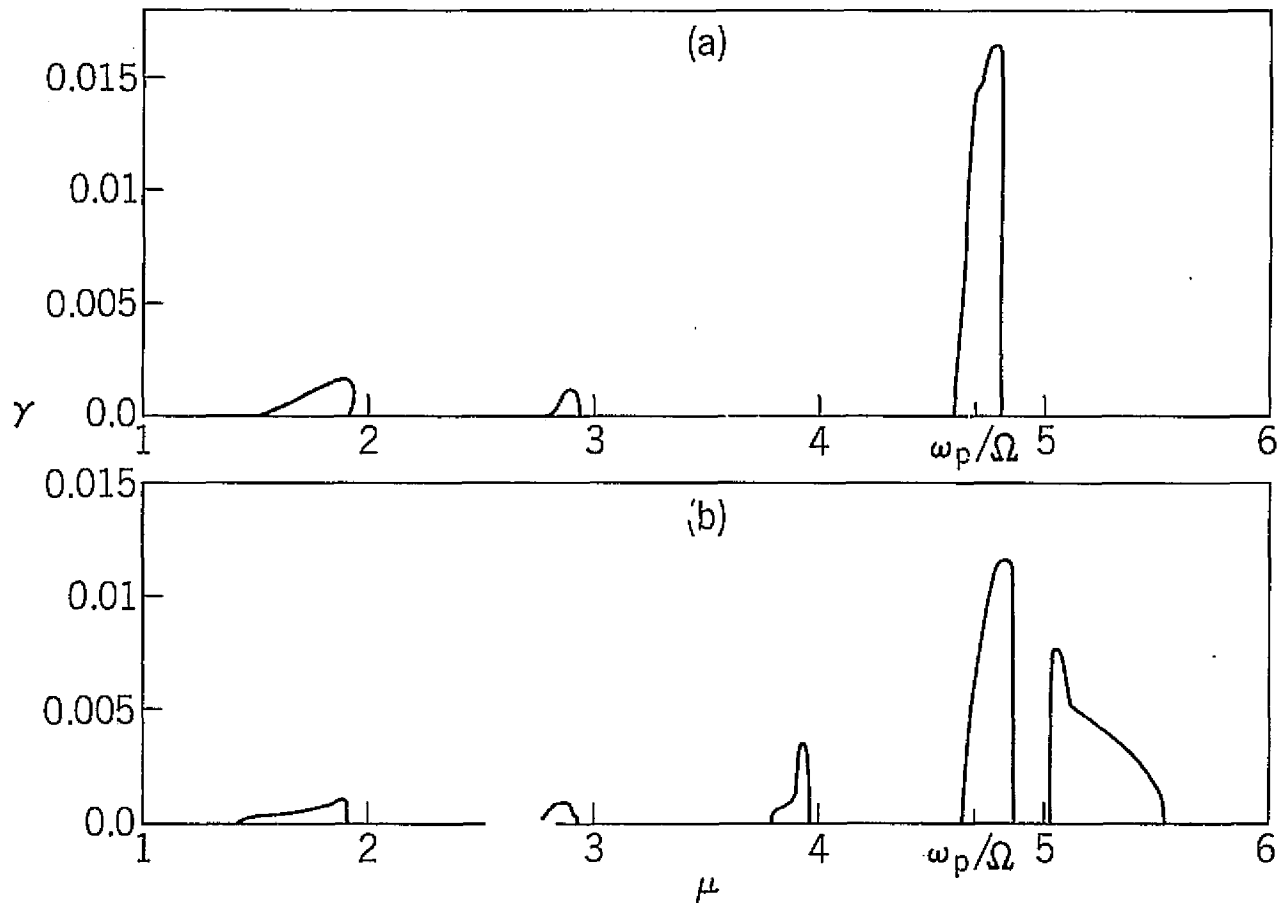


Figure 11. An example of gyroharmonic emissions near the plasma frequency. Fig. 11a gives  $\gamma$  vs.  $\mu$  for  $\beta = 10$ ,  $\Delta = 0$ ,  $\mu_{UH}^c = 4.58$ ,  $f_p/f_g = 4.69$ , and  $T_c/T_H = 0.01$ . The dominant feature is a single strong emission near  $f_p$ . In Fig. 11b,  $T_c/T_H = 0.02$ , and an emission band above  $5f_g$  would be seen. Class 5 emissions include both single band and multiple band emissions near  $f_p$ .



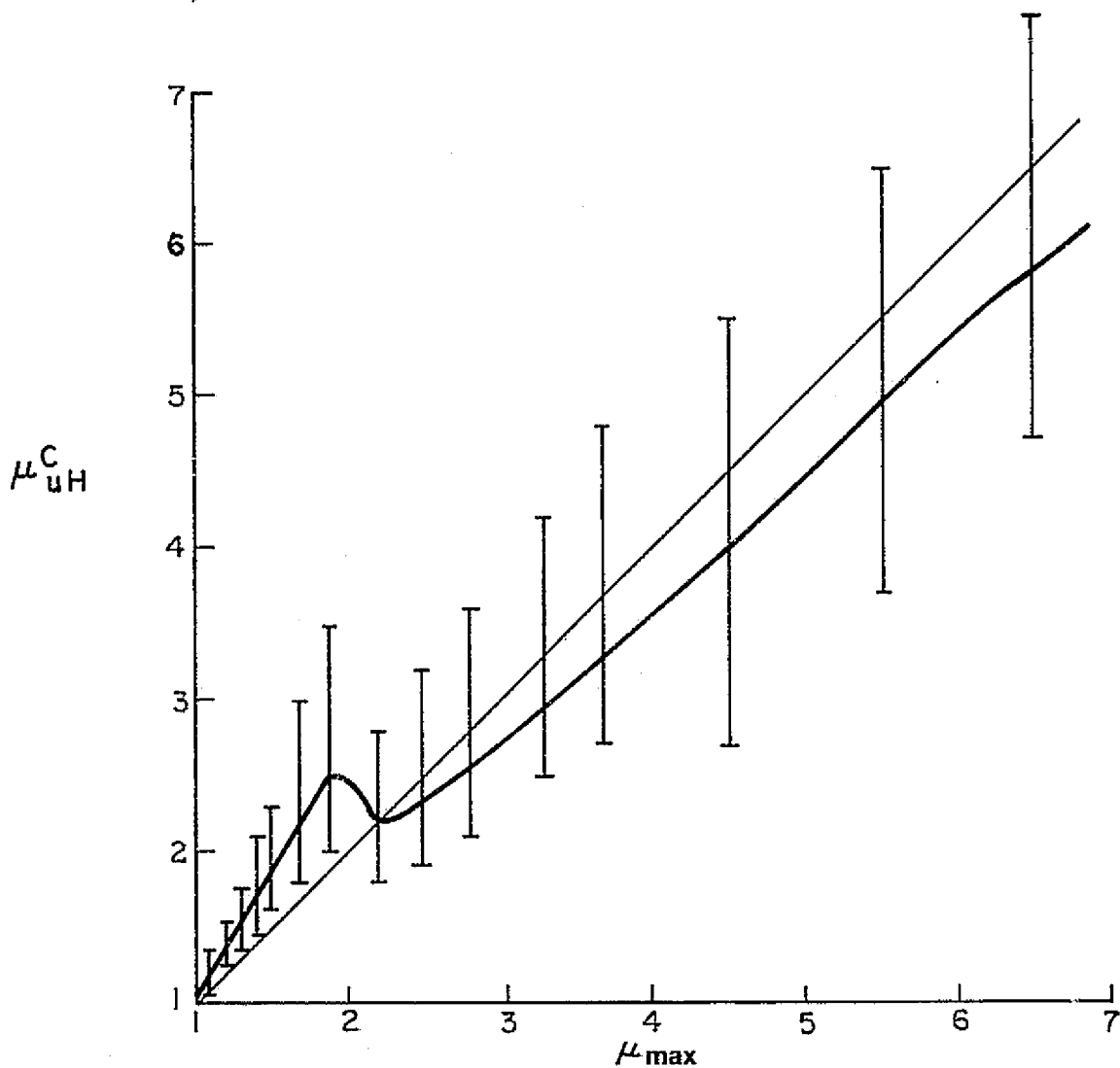


Figure 12. An estimate, based on solutions to the linear dispersion relation, of the cold upper hybrid frequency  $\mu_{UH}^C$  vs. maximum observed frequency  $\mu_{max}$ . The "error bars" are uncertainty estimates assuming  $\Delta < 0.05$ . This figure can be used to estimate  $\mu_{UH}^C$  from electric and magnetic field data whenever emissions of any class are observed.

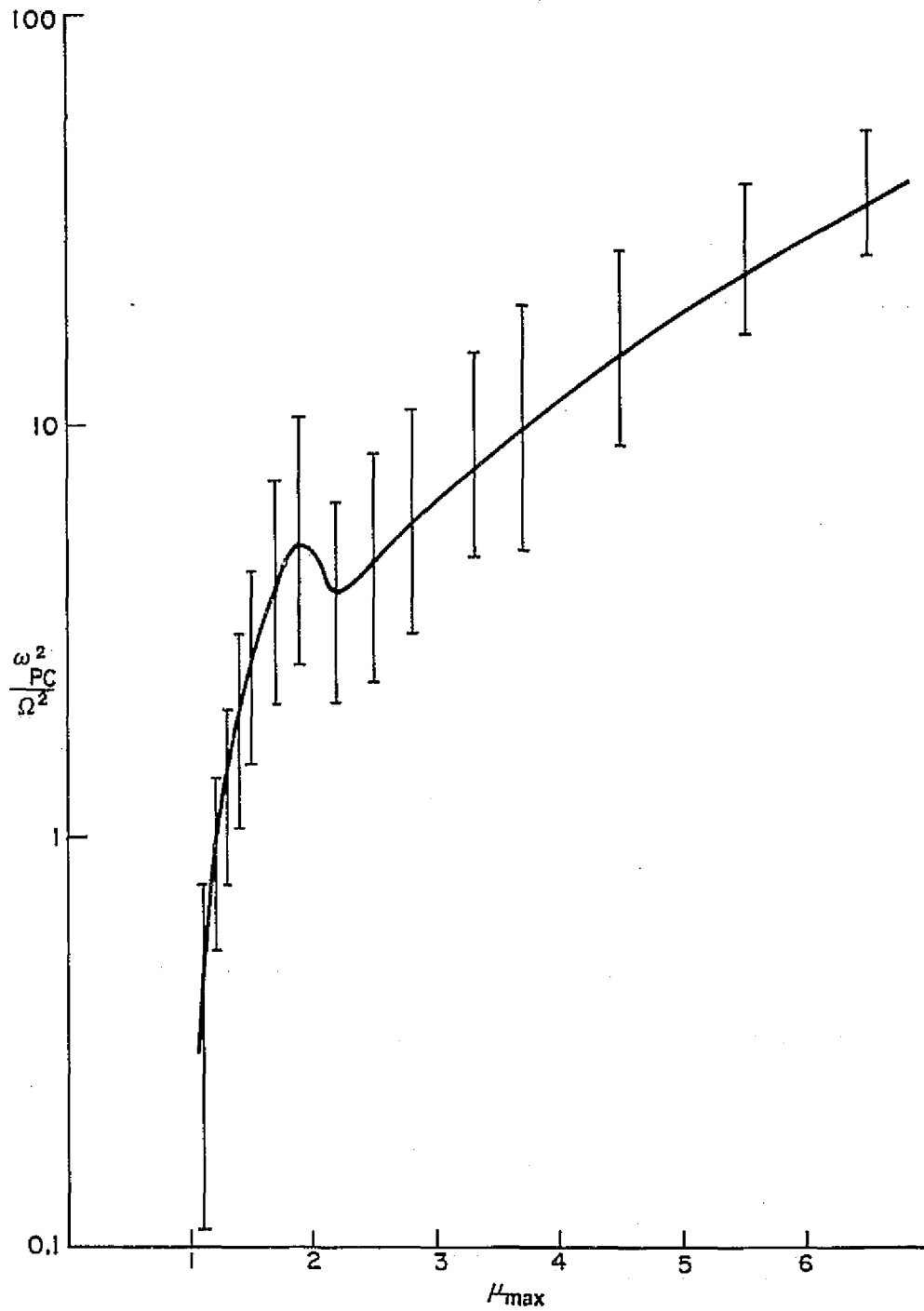


Figure 13. The estimates of Fig. 12 converted to  $\omega_{pc}^2/\Omega^2$  (or equivalently  $n_c$ ) vs. maximum observed frequency  $\mu_{max}$ . This figure can be used as a diagnostic tool to estimate the cold plasma density  $n_c$ .

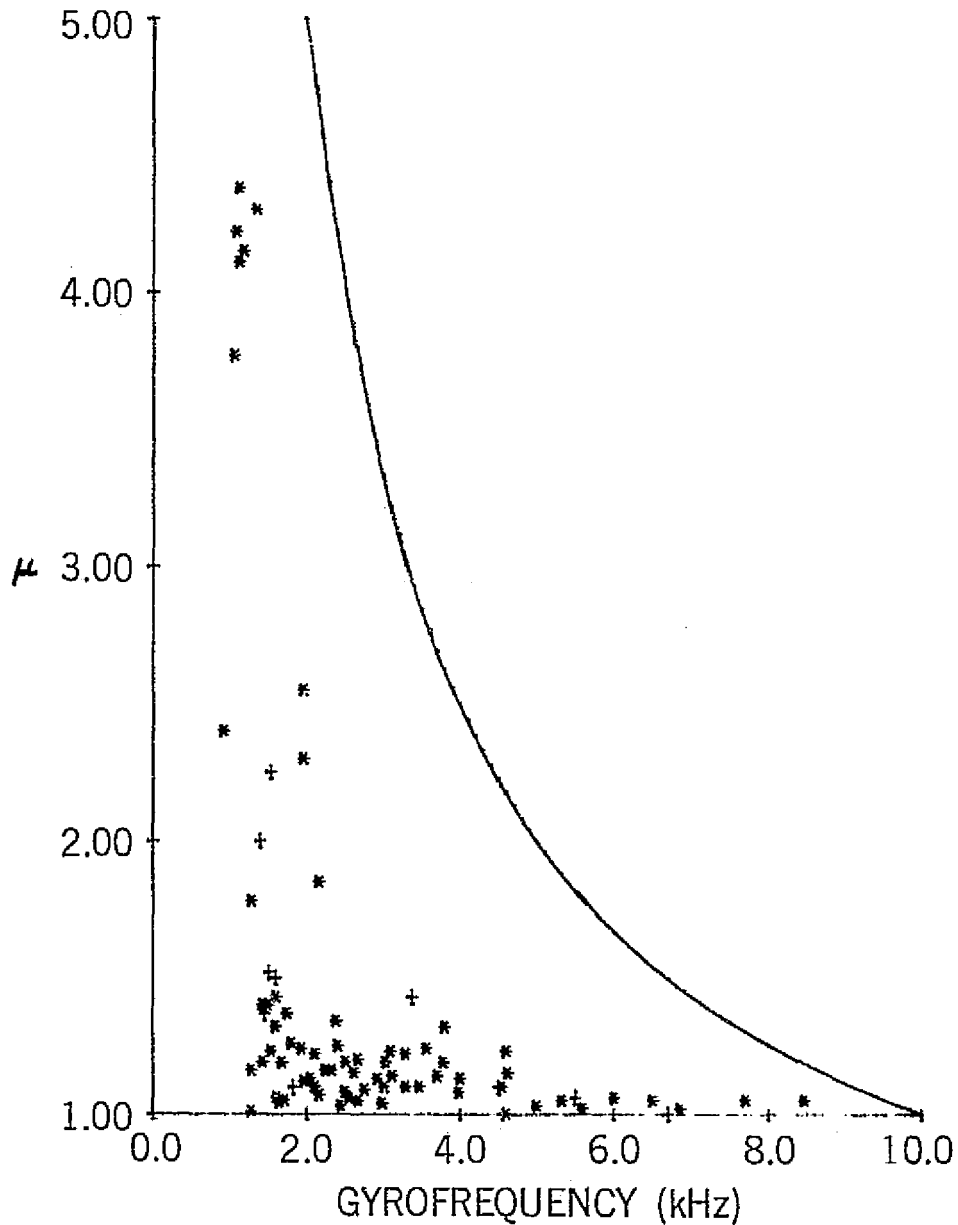


Figure 14. A plot of 83 individual electric field observations taken at 15 minute intervals from Imp 6 Orbits 178-183 whenever "odd-half-harmonic" emissions are seen. The graph shows the maximum observed frequency  $\mu_{\max}$  (in units of  $f_g$ ) vs.  $f_g$ . Higher relative frequencies tend to occur when the magnetic field is weakest, and almost all emissions between  $f_g$  and  $2f_g$  occur below  $1.5f_g$ . The region above the solid curve corresponds to frequencies above 10 kHz and cannot be observed in the data.

## APPENDIX A

### EVALUATION OF HOT ELECTRON CONTRIBUTION TO THE DISPERSION RELATION

Since  $f = f_H + f_c$ , the hot and cold electron components contribute separately to the dispersion equation, Eq. (1). We consider here the hot contribution

$$H_H = \frac{\Omega^2}{k^2} \sum_{n=-\infty}^{+\infty} \int_{-\infty}^{+\infty} dv_{\parallel} \frac{C_{nH} \frac{\partial f_{\parallel H}}{\partial v_{\parallel}} + n\Omega \frac{D_{nH}}{k_{\parallel}} f_{\parallel H}}{v_{\parallel} + \frac{n\Omega - \omega}{k_{\parallel}}} \quad (\text{A-1})$$

where the  $H_H$ -notation is that introduced in conjunction with Eq. (5), and we have partitioned

$$f_H = f_{\perp}(v_{\perp})f_{\parallel}(v_{\parallel})$$

We evaluate

$$C_{nH} = \frac{2}{\alpha_{\perp H}^2} \int_0^{\infty} dv_{\perp} v_{\perp} J_n^2 \left( \frac{k_{\perp} v_{\perp}}{\Omega} \right) \left[ \Delta + \frac{(1-\Delta)v_{\perp}^2}{\alpha_{\perp H}^2} \right] \exp - \frac{v_{\perp}^2}{\alpha_{\perp H}^2}$$

and find it equals

$$C_{nH} = \exp - \frac{\lambda_{\perp H}^2}{2} \left[ I_n \left( \frac{\lambda_{\perp H}^2}{2} \right) - \frac{(1-\Delta)}{2} \lambda_{\perp H}^2 (I_n - I_n') \right] \quad (\text{A-2})$$

where the  $I_n$ 's are modified Bessel Functions of order  $n$  and the notation

$\lambda_{\perp H} = k_{\perp} \alpha_{\perp H} / \Omega$  has been used. In a similar manner

$$\begin{aligned}
D_{nH} &= \frac{2}{\alpha_{\perp H}^2} \int_0^{\infty} dv_{\perp} I_n^2 \frac{\partial}{\partial v_{\perp}} \left\{ \left[ \Delta + \frac{(1-\Delta)v_{\perp}^2}{\alpha_{\perp H}^2} \right] \exp -\frac{v_{\perp}^2}{\alpha_{\perp H}^2} \right\} \\
&= \frac{1}{\alpha_{\perp H}^2} \exp -\frac{\lambda_{\perp H}^2}{2} \left[ -2\Delta I_n + (1-\Delta)\lambda_{\perp H}^2 (I_n - I_n') \right] \quad (A-3)
\end{aligned}$$

For the parallel integration we insert the Lorentzian form and define

$$\tilde{\mu}_n = \frac{\omega - n\Omega}{k_{\parallel}}$$

The first  $v_{\parallel}$ -integral in (1) thus becomes

$$Q_{n,p}^{\circ} \int_{-\infty}^{+\infty} dv_{\parallel} \frac{\partial f_{\circ} / \partial v_{\parallel}}{v_{\parallel} - \tilde{\mu}_n} = -2p N_p \int_{-\infty}^{+\infty} dv_{\parallel} \frac{v_{\parallel}}{(v_{\parallel}^2 + \alpha_{\parallel H}^2)^{p+1}} \frac{1}{v_{\parallel} - \tilde{\mu}_n} \quad (A-4)$$

where  $N_p$  denotes the normalization factor

$$N_p = \frac{1}{\pi} \frac{(2p-2)!!}{(2p-3)!!} (\alpha_{\parallel H})^{2p-1} \quad 0!! = (-1)!! \equiv 1$$

Note that  $Q_{n,p}^{\circ}$  may be written as

$$\begin{aligned}
Q_{n,p}^{\circ} &= \frac{2}{(p-1)!} (-1)^{p+1} \frac{N_p}{\alpha_{\parallel H}^{2p+1}} \frac{\partial^p}{\partial s^p} \int_{-\infty}^{+\infty} dx \frac{x}{(x^2 + s)} \frac{1}{x - \frac{\tilde{\mu}_n}{\alpha_{\parallel H}}} \Bigg|_{s=1} \\
&= 2^p \frac{(-1)^{p+1}}{(2p-3)!!} \frac{1}{\alpha_{\parallel H}^2} \frac{\partial^p}{\partial s^p} \frac{1}{\left( \sqrt{s} - \frac{i\tilde{\mu}_n}{\alpha_{\parallel H}} \right)} \Bigg|_{s=1} \quad (A-5)
\end{aligned}$$

the latter form of (A-5) following by contour integration-closing in the negative imaginary  $x$ -plane and picking up the contribution from the simple pole at  $x = -i\sqrt{s}$ . (According to our convention, integration in the complex  $\omega$ -plane is to be carried out with  $\text{Im } \omega > 0$ , so that for integration purposes  $\text{Im } \tilde{\mu}_n > 0$ .)

In exactly the same way we evaluate

$$\begin{aligned}
 Q_{n,p}^1 &= \int_{-\infty}^{+\infty} dv_{\parallel} \frac{f_{\parallel H}}{(v_{\parallel} - \tilde{\mu}_n)} = N_p \int_{-\infty}^{+\infty} dv_{\parallel} \frac{1}{(v_{\parallel}^2 + \alpha_{\parallel H}^2)^p} \frac{1}{(v_{\parallel} - \tilde{\mu}_n)} \\
 &= \frac{i 2^{p-1} (-1)^{p+1}}{(2p-3)!!} \frac{1}{\alpha_{\parallel H}} \frac{\partial^{p-1}}{\partial s^{p-1}} \left. \frac{1}{\sqrt{s} \left( \sqrt{s} - i \frac{\tilde{\mu}_n}{\alpha_{\parallel H}} \right)} \right|_{s=1} \quad (A-6)
 \end{aligned}$$

If one of the differentiations in (A-5) is carried out explicitly,  $H_H$  can be expressed in the particularly convenient form

$$\begin{aligned}
 H_H &= \frac{1}{\lambda_{\parallel H}^2} \frac{k_{\parallel}^2}{k^2} \frac{2^{p-1} (-1)^{p+1}}{(2p-3)!!} \frac{\partial^{p-1}}{\partial s^{p-1}} \left\{ \frac{1}{\sqrt{s}} \sum_n \frac{1}{\left( \sqrt{s} - \frac{i\tilde{\mu}_n}{\alpha_{\parallel H}} \right)} \right. \\
 &\quad \left. \left[ - \frac{C_{nH}}{\left( \sqrt{s} - \frac{i\tilde{\mu}_n}{\alpha_{\parallel H}} \right)} + \frac{i\alpha_{\parallel H}^2}{\lambda_{\parallel H}} n D_{nH} \right] \right\} \Bigg|_{s=1} \quad (A-7)
 \end{aligned}$$

If we define further

$$H_H^{p=1} = \frac{1}{\lambda_{\parallel H}^2} \frac{k_{\parallel}^2}{k^2} \frac{1}{\sqrt{s}} \sum_{n=-\infty}^{+\infty} \frac{1}{\left( \sqrt{s} - \frac{i\tilde{\mu}_n}{\alpha_{\parallel H}} \right)} \left[ - \frac{C_{nH}}{\left( \sqrt{s} - \frac{i\tilde{\mu}_n}{\alpha_{\parallel H}} \right)} + \frac{i\alpha_{\parallel H}^2}{\lambda_{\parallel H}} n D_{nH} \right]$$

so that

$$H_H = \frac{2^{p-1}(-1)^{p+1}}{(2p-3)!!} \left( \frac{\partial^{p-1}}{\partial s^{p-1}} H_H^{p=1} \right) \Big|_{s=1} \quad (\text{A-8})$$

then

$$\begin{aligned} H_H^{p=1} &= \frac{k_{\parallel}^2}{k^2} \frac{1}{\lambda_{\parallel H}^2} \frac{1}{\sqrt{s}} \exp - \frac{\lambda_{\perp H}^2}{2} \left[ \left[ \frac{\partial}{\partial \sqrt{s}} - \frac{1-\Delta}{2} \lambda_{\perp H}^2 \frac{\partial}{\partial \sqrt{s}} \left( 1 - \frac{\partial}{\partial z} \right) \right] \sum_{n=-\infty}^{+\infty} \frac{I_n}{\sqrt{s} - \frac{i\tilde{\mu}_n}{\alpha_{\parallel H}}} \right. \\ &\quad - \frac{i\alpha_{\parallel H}^2}{\alpha_{\perp H}^2} \frac{1}{\lambda_{\parallel H}} \Gamma \left[ 2\Delta - (1-\Delta)\lambda_{\perp H}^2 \left( 1 - \frac{\partial}{\partial z} \right) \right] \sum_{n=-\infty}^{+\infty} \frac{I_n}{\sqrt{s} - \frac{i\tilde{\mu}_n}{\alpha_{\parallel H}}} \\ &\quad \left. - \frac{2\Delta\alpha_{\parallel H}^2}{\alpha_{\perp H}^2} \exp \frac{\lambda_{\perp H}^2}{2} \right] \quad (\text{A-9}) \end{aligned}$$

In. Eq. (A-9)

$$\Gamma(\sqrt{s}) = \mu + i\sqrt{s}\lambda_{\parallel H}$$

and use has been made of the identity

$$\sum_{n=-\infty}^{+\infty} I_n \left( \frac{\lambda_{\perp H}^2}{2} \right) = \sum_{n=-\infty}^{+\infty} I'_n \left( \frac{\lambda_{\perp H}^2}{2} \right) = \exp \frac{\lambda_{\perp H}^2}{2}$$

We now proceed to evaluate the summation

$$\sum_{n=-\infty}^{+\infty} \frac{I_n(\lambda_{IH}^2/2)}{\left(\sqrt{s} - \frac{i\tilde{\mu}_n}{\alpha_{||H}}\right)} = i\lambda_{||H} \sum_{n=-\infty}^{+\infty} \frac{I_n(z)}{\Gamma - n} \quad (\text{A-10})$$

in the limit that  $z \rightarrow \infty$ . Note that

$$f(z, \Gamma) = \sum_{n=-\infty}^{+\infty} \frac{I_n(z)}{\Gamma - n} = -\frac{i}{1 - \exp 2\pi i \Gamma} \int_0^{2\pi} d\phi \exp(i\Gamma\phi + z \cos \phi) \quad (\text{A-11})$$

This result is most easily proven by working in the reverse direction, i. e., expanding  $\exp(z \cos \phi)$  in terms of a Bessel Series and performing then the  $\phi$ -integration. Further

$$f(z, \Gamma) = \frac{-i}{1 - \exp 2\pi i \Gamma} [g(z, \Gamma) + \exp 2\pi i \Gamma g(z, -\Gamma)]$$

where

$$g(z, \Gamma) = \int_0^{\pi} d\phi \exp(i\Gamma\phi + z \cos \phi) \quad (\text{A-12})$$

The form (A-12) is ideal for asymptotic analysis: for large  $z$ , the major contribution to the integral comes from a small region around  $\phi = 0$  where  $\cos \phi \cong 1$ , and we may series expand the cosine function

$$g(z, \Gamma) \cong \exp z \int_0^{\infty} d\phi \exp\left(i\Gamma\phi - \frac{z\phi^2}{2}\right) \left[1 + \frac{z\phi^4}{24} + \mathcal{O}(z\phi^6)\right] \quad (\text{A-13})$$



Convergence in (A-13) comes from the  $\exp - \frac{z\phi^2}{2}$  factor and has essentially occurred by the time  $\phi \sim \frac{\sqrt{2}}{z}$ . The  $\frac{z\phi^4}{24}$  term is then an  $\mathcal{O}\left(\frac{1}{z}\right)$  correction to the dominant term in (A-13). The  $\mathcal{O}(z\phi^6)$  correction is of  $\mathcal{O}\left(\frac{1}{z^2}\right)$  and still smaller. Extension of the upper integration limit to  $\infty$  introduces an error exponentially small in  $z$ . We retain the dominant and first non-dominant term in  $g$  and write

$$g(z, \Gamma) \cong \exp z \left(1 + \frac{z}{6} \frac{\partial^2}{\partial z^2}\right) \int_0^\infty d\phi \exp \left(i\Gamma\phi - \frac{z\phi^2}{2}\right) \\ = \frac{\sqrt{\pi}}{\Gamma} \exp z \left(1 + \frac{z}{6} \frac{\partial^2}{\partial z^2}\right) \left\{ \frac{\Gamma}{\sqrt{2z}} \exp - \frac{\Gamma^2}{2z} \left[1 + \operatorname{erf}\left(\frac{i\Gamma}{\sqrt{2z}}\right)\right] \right\} \quad (\text{A-14})$$

where the error function has its usual definition

$$\operatorname{erf}(x) = \frac{2}{\sqrt{\pi}} \int_0^x dt \exp - t^2$$

Carrying out the differentiation indicated in (A-14), we obtain

$$g(z, \Gamma) = \sqrt{\frac{\pi}{2z}} \exp z \left\{ \left[1 + \frac{1}{24z} \left(3 - 6 \frac{\Gamma^2}{z} + \frac{\Gamma^4}{z^2}\right)\right] \exp - \frac{\Gamma^2}{2z} \left[1 + \operatorname{erf}\left(\frac{i\Gamma}{\sqrt{2z}}\right)\right] \right. \\ \left. + \frac{i}{12\sqrt{\pi z}} \frac{\Gamma}{\sqrt{2z}} \left(5 - \frac{\Gamma^2}{z}\right) \right\} \quad (\text{A-15})$$

Finally we conclude

$$\sum_{n=-\infty}^{+\infty} \frac{I_n(z)}{\Gamma - n} = \exp \left(z - \frac{\Gamma^2}{2z}\right) \sqrt{\frac{\pi}{2z}} \left[ \frac{\sin 2\pi\Gamma}{1 - \cos \pi\Gamma} - i \operatorname{erf}\left(\frac{i\Gamma}{\sqrt{2z}}\right) \right] \left[1 + \frac{1}{24z} \left(3 - \frac{6\Gamma^2}{z} + \frac{\Gamma^4}{z^2}\right)\right] \\ + \frac{\exp z}{24z^2} \Gamma \left(5 - \frac{\Gamma^2}{z}\right) \quad (\text{A-16})$$

The leading order term is the one of order  $\frac{1}{\sqrt{z}}$ . The asymptotic smallness of corrections depends on  $\Gamma^2/z$  remaining of  $\mathcal{O}(1)$  or smaller as  $z \rightarrow \infty$ .

For  $\Gamma^2/z \sim \mathcal{O}(1)$  all correction terms in (A-16) are of comparable magnitude and are small compared to the dominant by the anticipated  $1/z$ .

We now incorporate the leading order term of Eq. (A-16) into Eq. (A-9). While it would appear that terms in (A-9) having  $\lambda_{IH}^2$  as a multiplicative factor are asymptotically dominant, operation by  $\left(1 - \frac{\partial}{\partial z}\right)$  drops their magnitude by one compensating order in  $\lambda_{IH}^2$ . We are justified in retaining only the lowest order term in (A-16) because neither the operations  $\frac{\partial}{\partial \sqrt{s}}$  nor  $\left(1 - \frac{\partial}{\partial z}\right)$  changes the relative ordering of the dominant and correction terms. Our final result is

$$\begin{aligned}
 H_H^{p=1} = & \frac{k_{\parallel}^2}{k^2} \frac{1}{\lambda_{\parallel H}^2} \frac{1}{\sqrt{s}} \left\{ \frac{\sqrt{\pi}}{\lambda_{\perp H}} \exp -\frac{\Gamma^2}{\lambda_{IH}^2} \left\langle \lambda_{\parallel H}^2 \left[ \left(1 - \frac{2\Gamma^2}{\lambda_{IH}^2}\right) \left(\frac{1-\Delta}{2}\right) - 1 \right] \frac{2\pi}{\cos 2\pi\Gamma - 1} \right. \right. \\
 & + \Gamma \frac{\alpha_{\parallel H}^2}{\alpha_{\perp H}^2} \left[ 2\Delta + (1-\Delta) \left(\frac{2\Gamma^2}{\lambda_{IH}^2} - 1\right) \right] \left[ \frac{\sin 2\pi\Gamma}{1 - \cos 2\pi\Gamma} - i \operatorname{erf} \left(\frac{i\Gamma}{\lambda_{IH}}\right) \right] \right\rangle \\
 & \left. - \frac{2\alpha_{\parallel H}^2}{\alpha_{\perp H}^2} \left[ \Delta + \frac{(1-\Delta)\Gamma^2}{\lambda_{IH}^2} \right] \right\}
 \end{aligned} \tag{A-17}$$

## APPENDIX B

### OUTLINE OF COMPUTER SOLUTION TO THE DISPERSION RELATION

We here discuss computational detail briefly beginning with a summary of our treatment of  $H_H$ . We choose initially values of  $\lambda_{\perp H}$ ,  $\alpha_{\perp H}/\alpha_{\parallel H}$ , and the propagation direction  $\theta = \tan^{-1} \frac{k_{\perp}}{k_{\parallel}}$ . Our work thus far has concentrated on the "isotropic" case  $\alpha_{\perp H} = \alpha_{\parallel H}$  and we discuss only these results. Given the values of these three chosen parameters,  $\lambda_{\parallel H}$  is determined. We next vary  $\mu_r$ , typically between  $\mu_r = 1.02$  and  $\mu_r = 5.98$ , in steps of .04, evaluating  $H_{H,real}^{p=1}$  and  $H_{H,imag}^{p=1}$  using the computer to sort real and imaginary parts. In the process we also compute the first three  $\mu_r$  derivatives of both the real and imaginary parts at each  $\mu_r$  value. We store these values of  $H_H$  and its derivatives on tape, tabulating separately the contributions of the "loss cone" and "filled in" components, which are characterized respectively by the multiplicative factors  $(1 - \Delta)$  and  $\Delta$  in Eq. (6). This table is then repeated for various pairs of  $\lambda_{\perp H}$  and  $\theta$ ,  $\lambda_{\perp H}$  typically varying between 2.5 and 16 in a variable step size ( $.5 \leq \Delta\lambda \leq 2$ ) and  $\theta$  taking on the values  $89.5^\circ$ ,  $88^\circ$ ,  $86^\circ$ ,  $82^\circ$ , and  $76^\circ$ .

We combine each tabulation of  $H_H$ , characterized by fixed  $\lambda_{\perp H}$ ,  $\theta$ , and  $\mu_r$ , with several "realizations" of cold plasma. In characterizing the cold plasma we still have the freedom to choose  $\beta$  and  $\alpha_c/\alpha_H$ . (Again, we have as yet considered only  $\alpha_{\parallel c} = \alpha_{\perp c}$ ). Once these parameters are chosen  $H_{c,real}$  and  $H_{c,imag}$

are calculated from Eq. (9). This procedure is a standard one, and further discussion of it will be omitted.

Finally  $\omega_{pH}^2/\Omega^2$  is evaluated from Eq. (10) and  $\mu_i$  and  $(\Delta\mu)_r$  are determined from Eq. (11). [ $\Delta\mu_r$  is typically  $<0.02$  for accepted results.]

While the sequential events of computation are as detailed above, parametric dependencies are ultimately determined by cross referencing. For example, one would determine the dependence of  $\mu_r$  and  $\mu_i$  on  $\lambda_{\perp H}$  (and hence  $\lambda_{\perp c}$ ) for fixed  $\theta, \beta$ , and  $\alpha_c/\alpha_H$  by first generating several tables each characterized by a different value of  $\lambda_{\perp H}$ . Each table would have as "output" the values of  $\omega_{pH}^2/\Omega^2, \mu_i$ , and  $(\Delta\mu)_r$  as a function of the "input"  $\mu_r$ . One would then further search from table to table at fixed  $\omega_{pH}^2/\Omega^2$  to determine, usually by interpolation  $\mu_i$  and  $\mu_r + (\Delta\mu)_r$  as functions of  $\lambda_{\perp}$ .